Dynamical density-functional-theory-based modeling of tissue dynamics: Application to tumor growth

Hayder M. Al-Saedi,[1,2] Andrew J. Archer,[1] and John Ward[1]
[1]*Department of Mathematical Sciences, Loughborough University, Loughborough LE11 3TU, United Kingdom*
[2]*Department of Mathematical Sciences, Baghdad University, Baghdad, Iraq*

(Received 1 March 2018; published 20 August 2018)

We present a theoretical framework based on an extension of dynamical density-functional theory (DDFT) for describing the structure and dynamics of cells in living tissues and tumors. DDFT is a microscopic statistical mechanical theory for the time evolution of the density distribution of interacting many-particle systems. The theory accounts for cell-pair interactions, different cell types, phenotypes, and cell birth and death processes (including cell division), to provide a biophysically consistent description of processes bridging across the scales, including describing the tissue structure down to the level of the individual cells. Analysis of the model is presented for single-species and two-species cases, the latter aimed at describing competition between tumor and healthy cells. In suitable parameter regimes, model results are consistent with biological observations. Of particular note, divergent tumor growth behavior, mirroring metastatic and benign growth characteristics, are shown to be dependent on the cell-pair-interaction parameters.

DOI: 10.1103/PhysRevE.98.022407

I. INTRODUCTION

One of the characteristics of biological systems is their ability to produce and sustain spatiotemporal patterns—i.e., structure formation. Cancer is a disease that may be viewed as a complex system whose dynamics and growth results from nonlinear processes coupled across a wide range of spatiotemporal scales. Cancer is recognized as one of the major causes of premature death, soon to overtake heart disease as the leading cause in the developed nations [1]. At current rates, in the U.S.A. a third of women and half of men will develop a cancer at some point in their life [2]. Though significant progress has been made in cancer treatment in recent decades, much research is still required to control all forms of the disease.

The human body is made up of order 10^{13} cells. Genetic mutations are frequent, but most affected cells die by apoptosis and are removed by the immune system. However, a few may escape the regulatory process to produce an abnormally growing colony that in time recruits its own vascular system (via angiogenesis) and form a cancer. Tumor growth varies and solid tumors can be classified as either benign or malignant [3]. The former are localized, but their continued growth can cause damage to neighboring healthy tissues from the mechanical forces applied. While most tumors are initially benign, malignancy can develop, whereby individual cells are able to escape the main tumor mass (metastasis) and colonize elsewhere in the body; it is these cells that give rise to the greatest clinical concern.

Much work has gone into developing mathematical models of cancers. Of particular interest here is the spatiotemporal dynamics, which can be described, e.g., using continuum, discrete, and hybrid models. Continuum approaches usually result in a system of coupled partial differential equations and have been used to describe avascular growth [4–10], vascular growth [4,11–14], angiogenesis [15–17], and treatment [18–20]. Most of these consider the overall growth as being dependent on nutrient(s) that diffuses in from the outside, while more sophisticated extensions of these models treat the tumor as a poroviscous [21–23] or poroelastic [11,15,24,25] structure. In such models, the cell-cell interactions enter via coefficients in the mass conservation terms and (usually) linear constitutive relations describing the macroscale material properties of the tissue, rather than via any genuine microscale description of the interaction between cells. Of course, the advantage of such models is that they are amenable to analytical techniques and relatively small-scale computation. However, the microscopic cell-cell interactions play a crucial role in the development and function of multicellular organisms [26], so it is desirable to incorporate cell-cell interaction effects in the modeling. These interactions determine the structural integrity of tissue and allow cells to communicate with each other in response to changes in their microenvironment, which is essential for the survival of the cells and the host. Such communication includes that from physical contact and chemical signals, transported directly through gap junctions between cells or by passive diffusion. Some of these aspects can differ between healthy and cancer cells, so modeling these differences can be important.

Greater detail of the cell-cell interactions are routinely incorporated in discrete models for tumor growth, such as cellular-automata [27–29], agent-based models [30–32], and Potts models [33–35]. In these, cells are described at a microscopic level as entities that move and respond to neighbors via a set of biologically motivated rules. Simulating the action of a group of many of these cells then gives the evolution of a tumor on the macroscale. Cellular automata models consists of a regular grid of cells, each in one of a finite number of states, such as "on" or "off." In agent-based models their actions typically follow discrete event cues or a sequential schedule of interactions, rather than simultaneously performing actions at

constant time steps, as in cellular automata models. Potts-type models are able to incorporate how internal elements of the cells respond to one another based on certain characteristics that each possesses [28,32,34]. Though discrete models are good for incorporating the biology and physics of cell-cell interactions, they are designed for computation and are generally difficult to study analytically.

A continuum theory that also incorporates the cell-cell interactions at a microscopic level was proposed (but not analyzed) in Ref. [36]. The central idea is to base the model on dynamical density functional theory (DDFT) [37–39], which is a theory for the dynamics of interacting Brownian (colloidal) particles, able to describe the time evolution of the density distribution of the particles over length scales comparable with the size of the individual particles. This is the approach we extend and implement here. DDFT provides a systematic means of obtaining a continuum description of the density distribution of the cells that also incorporates a description of the microscale interactions between cells. One can solve the DDFT numerically for large enough systems to enable a macroscopic description at the population level, but perhaps more importantly is that it is amenable to mathematical analysis (e.g., determination of linear stability thresholds) providing further insight to the population collective behavior. DDFT is itself based on equilibrium density functional theory (DFT), an approach that has long been used to describe the structure of matter, be it (crystalline) solid, liquid, or gas [40–42]. We analyze in detail a version of the DDFT proposed in Ref. [36] (here we specify a particular model for the interaction potential between cells) and also extend the model to describe the dynamics of systems representing multiple cell types, incorporating the various different pair interactions between pairs of healthy cells, between pairs of cancer cells and the cancer-healthy pair interaction. The DDFT we use is based on a DFT able to describe both the fluid and (crystalline) solid phases of soft particles. In the latter, the density distribution corresponds to a regular array of peaks, defining where the particles are located. It is in this regime, where the peaks represent the loci of cell centers, that the theory is relevant to describing the microscopic density distribution of both cancer and healthy cells, which are treated as soft particles.

This paper is laid out as follows: In Sec. II we present the DDFT for a single species of cells, perform a linear stability analysis, and present some typical simulation results. In Sec. III we extend this model to describe the competition between cancer and healthy cells and again elucidate the behavior of the model using a linear stability analysis and simulations. Finally, in Sec. IV, we present our conclusions.

II. MODEL FOR A SINGLE SPECIES OF CELLS

A. Dynamical density functional theory

DDFT [37–39] is a theory for the spatiotemporal evolution of the ensemble average number density distribution $\rho(\mathbf{r},t)$ of a system of interacting Brownian particles, where t is the time and $\mathbf{r}$ is the position in space. The theory shows that the dynamics is given by

$$\frac{\partial\rho(\mathbf{r},t)}{\partial t}=\Gamma\nabla\cdot\left[\rho(\mathbf{r},t)\nabla\left(\frac{\delta\mathcal{F}[\rho(\mathbf{r},t)]}{\delta\rho(\mathbf{r},t)}\right)\right], \tag{1}$$

where Γ is a mobility coefficient and

$$\mathcal{F}[\rho(\mathbf{r})]=k_BT\int d\mathbf{r}\rho(\mathbf{r})(\ln[\Lambda^d\rho(\mathbf{r})]-1)+\mathcal{F}_{\rm ex}[\rho(\mathbf{r})]+\int d\mathbf{r}V_{\rm ext}(\mathbf{r})\rho(\mathbf{r}) \tag{2}$$

is the Helmholtz free-energy functional from equilibrium DFT [40–42]. The first term in Eq. (2) is the ideal gas contribution to the free energy, d is the dimensionality of space, k_B is Boltzmann's constant, T is the temperature, Λ is the thermal de Broglie wavelength, $V_{\rm ext}(\mathbf{r})$ is the external potential, and $\mathcal{F}_{\rm ex}[\rho(\mathbf{r})]$ is the excess contribution due to the interactions between particles. In general, $\mathcal{F}_{\rm ex}[\rho(\mathbf{r})]$ is not known exactly. However, there are many different approximations which may be used [41,42], with some being more appropriate than others, depending on the nature of the interactions between the fluid particles.

The equilibrium properties of the system are obtained by minimizing the grand potential functional,

$$\Omega[\rho(\mathbf{r})]=\mathcal{F}[\rho(\mathbf{r})]-\mu\int d\mathbf{r}\rho(\mathbf{r}), \tag{3}$$

where μ is the chemical potential, which is effectively the Lagrange multiplier that enforces the constraint that the average number of particles in the system is $N=\int d\mathbf{r}\rho(\mathbf{r})$. Note that Eq. (1) also enforces this constraint due to having the form of a continuity equation.

The equation of motion for each of the N interacting particles (cells) that is assumed in deriving Eq. (1) is the following over-damped Langevin equation,

$$\frac{d\mathbf{r}_i}{dt}=\Gamma\left(\mathbf{F}_i^{\rm ext}+\sum_{j=1}^{N}\mathbf{F}_{ij}^{\rm int}\right)+\sqrt{2D}\boldsymbol{\eta}_i(t), \tag{4}$$

where $\mathbf{r}_i$ is the position of the center of mass of the ith particle and $D=\Gamma k_BT$ is the diffusion coefficient. This assumes no cell-cell friction; incorporating such friction would involve the inclusion of an additional viscous drag force in the Langevin equation. The force $\mathbf{F}_i^{\rm ext}=-\nabla V_{\rm ext}(\mathbf{r}_i,t)$ is the force due to the external potential, e.g., due to any confining structures present, and the force $\mathbf{F}_{ij}^{\rm int}=-\nabla V_{\rm int}(\mathbf{r}_i-\mathbf{r}_j)$ is cell-cell interaction force between particles i and j, that is assumed to be governed by the pair potential $V_{\rm int}$ that depends on the distance between the two cells. The vector $\boldsymbol{\eta}_i(t)$ is a Gaussian random noise with components $\eta_i^\alpha(t)$ satisfying $\langle\eta_i^\alpha(t)\rangle=0$ and $\langle\eta_i^\alpha(t)\eta_j^\beta(t')\rangle=\delta_{ij}\delta_{\alpha\beta}\delta(t-t')$, where $\langle\cdot\rangle$ denotes a statistical average over different noise, realisations, δ_{ij} and $\delta_{\alpha\beta}$ are Kronecker deltas, $\delta(t-t')$ is a Dirac delta function and α, β are coordinate indices.

B. Extension to describe living cells

As discussed in Ref. [36], if living cells [density $\rho(\mathbf{r},t)$] are treated as interacting Brownian particles, then an equation for the time evolution of the density of the form of Eq. (1) is appropriate. However, since the cells can reproduce and die, there is an additional term $D_{\rm BD}^{(1)}[\rho(\mathbf{r})]$ added to the right-hand side of Eq. (1) to describe the nonconserved component of the dynamics due to birth and death (BD) processes.

As a simple model of BD, we assume that a single cell can undergo mitosis with a nutrient-dependent rate $a_m = a_m(n)$, where $n(\mathbf{r}, t)$ is the local concentration of nutrient (e.g., dissolved O_2). We model cell death (apoptosis) as occurring with a rate constant λ_d. This can be implemented as a Markov process and affects the number of cells in the population $N = N(t)$ [36]. The nutrient is provided by the vascular system, diffuses through the system, and is taken-up by the cells, and thus satisfies the reaction-diffusion equation

$$\frac{\partial n(\mathbf{r}, t)}{\partial t} = D_n \nabla^2 n(\mathbf{r}, t) + S_n f(\mathbf{r}) - \lambda_n \rho(\mathbf{r}, t) n(\mathbf{r}, t), \quad (5)$$

where D_n is the nutrient diffusion coefficient, S_n represents the amplitude of the nutrient source, and $f(\mathbf{r})$ is a function that defines where in space the nutrient source is located. Here, we consider both a uniform source $f(\mathbf{r}) = 1$ and a localized source in the form of Gaussian, namely,

$$f(\mathbf{r}) = e^{-(x-L/2)^2}, \quad (6)$$

which corresponds to a source of nutrient along the line $x = \frac{L}{2}$, where L is the domain width, e.g., due to a capillary being there. Here, λ_n is a nutrient uptake rate constant. The term in Eq. (5) describing this process is assumed to be proportional to n. From the fact that the first moment of the BD process is the result of two mass action laws gives $D^{(1)}_{\mathrm{BD}}[\rho] = a_m(n)\rho - \lambda_d \rho$, where $a_m(n)$ is a nutrient-dependent growth rate and λ_d is a death rate constant. We assume that $a_m(n) = \lambda_m n$, where λ_m is constant.

As a simple model for the cell-cell forces, we assume the cells interact via a soft, purely repulsive, and radially symmetric pair potential,

$$V_{\mathrm{int}}(r) = \varepsilon \exp[-(r/R)^{\mathcal{N}}], \quad (7)$$

where r is the distance between the centers of the cells and the parameters ε and R are the cell-cell interaction energy and cell radius, respectively, defining the strength and range of the potential. This is the so-called generalized exponential model with exponent $\mathcal{N}$, or "GEM-$\mathcal{N}$" potential [43]. Here, we set the exponent $\mathcal{N} = 4$. Such soft potentials arise as the coarse-grained effective potential between soft polymeric macromolecules in solution [43–51]. In this study, the parameter R typically represents the radius of a cell, so cells repulse each other when the distance between their centres are less than $2R$. While this property of V_{int} is necessary for biological relevance, longer range effects (for distances $\geqslant 2R$), such as cell-cell adhesion [30,32,35], can be straightforwardly built in to the interaction function [40–42]. Note also that whilst adhesion is important for maintaining cohesion, the structure of condensed systems is dominated by the interparticle repulsions [42].

We consider this model because the bulk structure and phase behavior of the GEM-$\mathcal{N}$ systems are well understood in both two dimensions (2D) and three dimensions, and also the following simple approximation for the excess free energy functional is fairly accurate and widely used [43,52–60],

$$\mathcal{F}_{\mathrm{ex}}[\rho(\mathbf{r})] = \frac{1}{2}\int d\mathbf{r} \int d\mathbf{r}' \rho(\mathbf{r})\rho(\mathbf{r}')V_{\mathrm{int}}(|\mathbf{r} - \mathbf{r}'|). \quad (8)$$

Taking the functional derivative and then substituting the result into the extension of Eq. (2), including the BD term described above, we obtain

$$\frac{\partial \rho(\mathbf{r}, t)}{\partial t} = \nabla \cdot \left[\Gamma \rho(\mathbf{r}, t) \nabla \left[k_B T \ln(\Lambda^d \rho(\mathbf{r}, t)) + \int d\mathbf{r}' \rho(\mathbf{r}', t) V_{\mathrm{int}}(|\mathbf{r} - \mathbf{r}'|) \right] \right] + [\lambda_m n(\mathbf{r}, t) - \lambda_d]\rho(\mathbf{r}, t). \quad (9)$$

The coupled pair, Eqs. (9) and (5), define our model for a single type of cells coupled to a source of nutrients. The parameters and their estimated values are listed in Table I. See also the Appendix, where we justify the particular values we use here. For simplicity, we henceforth assume the system is 2D within a square domain of area L^2 with periodic boundary conditions. Thus, $\mathbf{r} = (x, y)$. Two key quantities for understanding the behavior of the system are the average cell and nutrient densities in the domain defined as

$$\bar{\rho}(t) = \frac{1}{L^2}\iint \rho(x, y, t) dx dy, \quad (10)$$

$$\bar{n}(t) = \frac{1}{L^2}\iint n(x, y, t) dx dy, \quad (11)$$

respectively.

TABLE I. Model parameters and their units. Values marked with an asterisk (*) are estimates from the Appendix.

Symbol	Typical value	Unit	Source
$\rho(\mathbf{r}, t)$	$3\times10^{5*}$	cm^{-2}	Estimated
$n(\mathbf{r}, t)$	3^*	mg/L	Estimated
$V_{\mathrm{int}}(r)$	ε	Joule	Estimated
$N(t)$	$\rho_0 L^2$	Dimensionless	Sec. II E
R	0.001	cm	[61]
λ_m	0.00015^*	$\mathrm{L\ min^{-1} mg^{-1}}$	Estimated
λ_d	0.00005^*	min^{-1}	Estimated
λ_n	3^*	min^{-1}	Estimated
D_c	$1.3\times10^{-9*}$	$\mathrm{cm^2 min^{-1}}$	Estimated
D_n	0.0012	$\mathrm{cm^2 min^{-1}}$	[9]
Γ	$3\times10^{10*}$	$\mathrm{min\ g^{-1}}$	Estimated
T	310	K	[61]
k_B	1.38×10^{-23}	Joule/K	[62]
ε	$\approx k_B T$	Joule	Estimated
ρ_0	$3\times10^{5*}$	cm^{-2}	Sec. II E
L^2	6×10^{-4}	cm^2	Sec. II E
S_n	433^*	$\mathrm{mg\ L^{-1} min^{-1} cm^{-2}}$	Estimated

C. Nondimensionalization

We now nondimensionlize the model before performing a linear stability analysis and presenting some typical numerical results. Writing

$$t = \frac{R^2 t^*}{D_c}, \quad x = \frac{x^*}{R}, \quad y = \frac{y^*}{R}, \quad \rho = \frac{\rho^*}{R^2}, \quad n = \frac{\lambda_d n^*}{\lambda_m},$$
$$V_{\mathrm{int}}(r/R) = \varepsilon \tilde{V}_{\mathrm{int}}(r^*), \quad (12)$$

where the asterisked quantities are dimensionless variables, $D_c = \Gamma k_B T$ is the dimensional coefficient of diffusion of cells and $\tilde{V}_{\mathrm{int}}(r) = \exp(-r^{\mathcal{N}})$ is the dimensionless pair potential.

TABLE II. Dimensionless parameter values of the model.

Dimensionless param.	Dimension form	Value	Used value
c_1	$R^2\lambda_d/D_c$	0.038	1
$\tilde{D}$	D_n/D_c	10^6	1, 10, 10^2
$\tilde{S}_n$	$R^2 S_n\lambda_m/\lambda_d D_c$	10^6	10,35
$\tilde{\lambda}_n$	λ_n/D_c	10^6	1
$\beta\varepsilon$	$\beta\varepsilon$	O(1)	1

We also define the dimensionless parameters

$$c_1 = \frac{R^2\lambda_d}{D_c}, \quad \tilde{D} = \frac{D_n}{D_c}, \quad \tilde{S}_n = \frac{R^2 S_n\lambda_m}{\lambda_d D_c}, \quad \tilde{\lambda}_n = \frac{\lambda_n}{D_c}. \quad (13)$$

With these, we obtain the following nondimensional pair of coupled equations

$$\frac{\partial\rho(\mathbf{r},t)}{\partial t} = \nabla^2\rho(\mathbf{r},t) + \nabla\cdot\left(\rho(\mathbf{r},t)\nabla\int d\mathbf{r}'\rho(\mathbf{r}',t)\beta\varepsilon\tilde{V}_{int}(|\mathbf{r}-\mathbf{r}'|)\right) + c_1[n(\mathbf{r},t)-1]\rho(\mathbf{r},t), \quad (14)$$

$$\frac{\partial n(\mathbf{r},t)}{\partial t} = \tilde{D}\nabla^2 n(\mathbf{r},t) + \tilde{S}_n f(\mathbf{r}) - \tilde{\lambda}_n\rho(\mathbf{r},t)n(\mathbf{r},t), \quad (15)$$

where we have dropped the asterisks for clarity. Note that $\beta = 1/k_BT$ so that the dimensionless quantity $\beta\varepsilon$ in the integral term is the dimensionless pair interaction energy.

Our estimated values for the various dimensionless parameters in the model are listed in Table II. We note that the ratio of diffusion coefficients $\tilde{D}$ in Eq. (13) is large, which means that quantities in Eqs. (14) and (15) take dimensionless values covering several order of magnitudes O(10^{-2})–O(10^6). This is because the nutrient density distribution evolves on much faster timescales than the cells, which creates challenges for the numerical methods that we use below. Since the algorithm must run over a long time, the (nutrient) terms associated with the O(10^6) parameters equilibrate very rapidly by a time $t\sim$O(10^{-6}), compared to the slower (cells evolution) processes which take times $t\sim$O(10^2). Consequently, tempering the large valued parameters, say by setting $(10^6)\mapsto 1$ for the large parameters, has little effect on the long-term results but greatly helps in the running of the numerical code. We therefore select the parameter set given in Table II and henceforth use these as our standard parameter set. We also present results below, illustrating how the long-time results for $\rho(\mathbf{r},t)$ depend only very weakly on the value of $\tilde{D}$, as it is varied in the range $1\leqslant\tilde{D}\leqslant 10^2$.

D. Linear stability analysis

For $\tilde{S}_n > 0$ and $f(\mathbf{r})$=1 there is a unique uniform density steady state that is a stationary solution of Eqs. (14) and (15), that is

$$n = n_0 = 1, \quad \rho = \rho_0 = \tilde{S}_n/\tilde{\lambda}_n. \quad (16)$$

We now investigate the linear stability of the uniform density state (ρ_0, n_0) to nonuniform perturbations $[\delta\rho(\mathbf{r},t), \delta n(\mathbf{r},t)]$, with $\|\delta\rho\|_\infty = \xi$ and $\|\delta n\|_\infty = \chi\xi$, where $\xi \ll 1$. The analysis also applies more generally to determine the growth or decay of a perturbation about a uniform density state (ρ_0, n_0), with values different to those in Eq. (16), i.e., the timescale for cell repositioning in response to the perturbation is much faster than cell growth; we note $c_1 \ll 1$ from data, see Table II. Note that it is the parameter values where the uniform system is unstable (and forms peaks) that are of relevance biologically.

To determine the linear stability of the flat state, we assume that the cell density profile take the form

$$\rho = \rho_0 + \delta\rho(\mathbf{r},t) = \rho_0 + \xi e^{i(\mathbf{k}\cdot\mathbf{r})+\omega t}, \quad (17)$$

and the nutrient density profile

$$n = n_0 + \delta n(\mathbf{r},t) = n_0 + \chi\xi e^{i(\mathbf{k}\cdot\mathbf{r})+\omega t}, \quad (18)$$

where $0<\xi\ll 1$ is the initial amplitude of the sinusoidal perturbation that has wave number $k=|\mathbf{k}|$, χ is the ratio between the amplitude of the modulation in the two components, and the growth or decay rate of the perturbations is given by the dispersion relation $\omega=\omega(k)$. Substitution of Eqs. (17) and (18) into the dynamic Eq. (14), and then linearizing in $\delta\rho$, we obtain (cf. Refs. [38,60])

$$\omega(k) = -k^2[1+\rho_0\beta\varepsilon\hat{V}(k)] + c_1(n_0+\rho_0\chi-1), \quad (19)$$

where $\hat{V}(k)$ is the Fourier transform of the pair potential. Since we have assumed the system is in 2D, the Fourier transform is

$$\hat{V}(k) = \int d\mathbf{r}e^{i\mathbf{k}.\mathbf{r}}\tilde{V}_{\rm int}(\mathbf{r}) = 2\pi\int_0^\infty r\tilde{V}_{\rm int}(r)J_0(kr)dr, \quad (20)$$

where $J_0(x)$ is the Bessel function of order 0.

The limit of linear stability is defined as the locus of points in parameter space, where the maximum in the dispersion relation Eq. (19) is at zero, i.e., $\omega(k=k_c)=0$, where k_c is the wave vector where $\omega(k)$ is maximum, where $\frac{d\omega}{dk}|_{k=k_c}=0$. In the case of $c_1\ll 1$, we have

$$1+\rho_0\beta\varepsilon\hat{V}(k=k_c)\approx 0, \quad (21)$$

where $k_c\approx 5.1$ and $\hat{V}(k_c)\approx -0.16$ (recall that in the nondimensionalization we effectively set the unit of length $R=1$), which implies that the locus of where the system becomes linearly unstable is

$$\rho_0 \approx \frac{1}{\beta\varepsilon|\hat{V}(k_c)|}, \quad (22)$$

which in the density ρ_0 versus "dimensionless temperature" $k_BT/\varepsilon = 1/\beta\varepsilon$ plane is a straight line passing through the origin [60]. For densities greater than this value, the system is linearly unstable. Note that even though we have assumed $c_1\ll 1$ in the derivation, it turns out that even for $c_1 = O(1)$, Eq. (22) gives a good estimate for where the system is linearly unstable. Given the data in Table II, the analysis suggests that dominant terms governing instability is the cell density and the cell-cell interaction parameters; cell growth and nutrient consumption rates are secondary to this process.

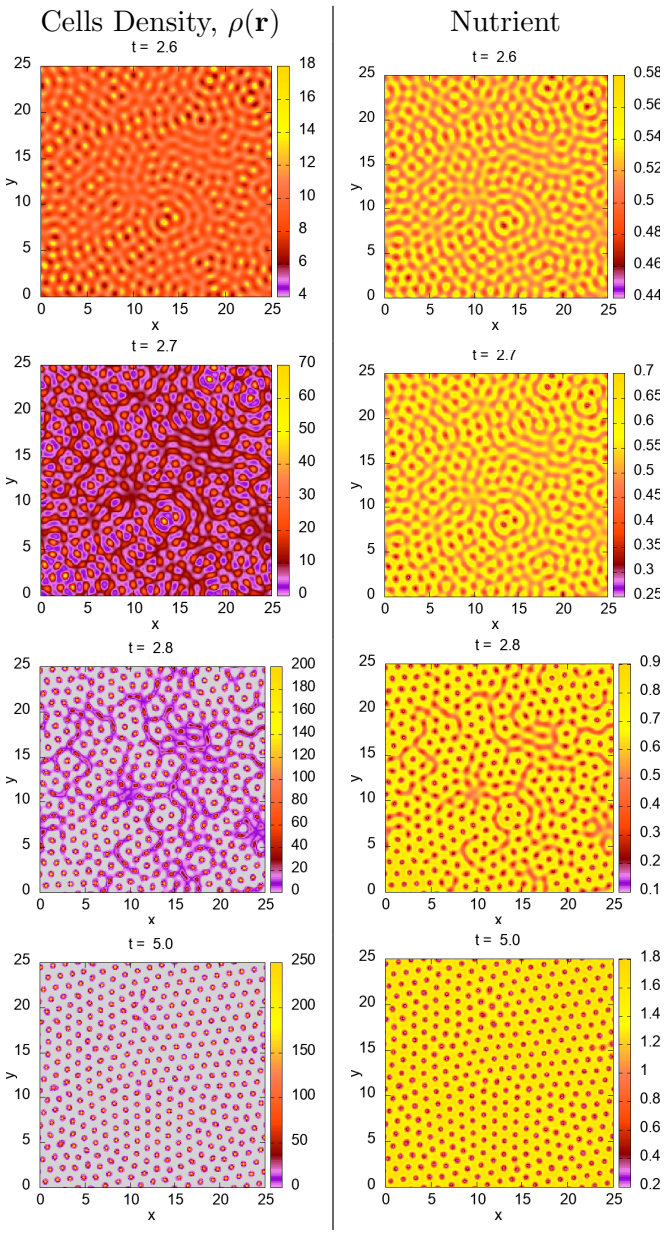

FIG. 1. Density of the cells (left) and local nutrition concentration (right) over time. We assume that the population growth constant $c_1 = 1$ and the energy scale in the interaction potential between cells $\beta\varepsilon = 1$. The diffusion coefficient ratio $\tilde{D} = 1$. The nutrient source is homogeneous with $f(\mathbf{r}) = 1$ and $\tilde{S}_n = 10$, and the nutrient uptake rate $\tilde{\lambda}_n = 1$. The area of the domain is 25.6^2 and $\Delta x = 0.1$.

E. Numerical results for the cell evolution

The coupled Eqs. (14) and (15) are solved numerically using the method of lines. The density profiles are discretized on a spatially uniform grid, with the convolution integral evaluated in Fourier space using fast Fourier transforms, while for the time stepping the Adam-Bashforth method is implemented, via the freeware ODEPACK routine DLSODE [63,64]. We note that this time-stepping method is significantly faster than the Euler time-stepping routines used for the similar problem in Ref. [60]. We note that all quantities shown in the figures, including those of Sec. III D, are dimensionless.

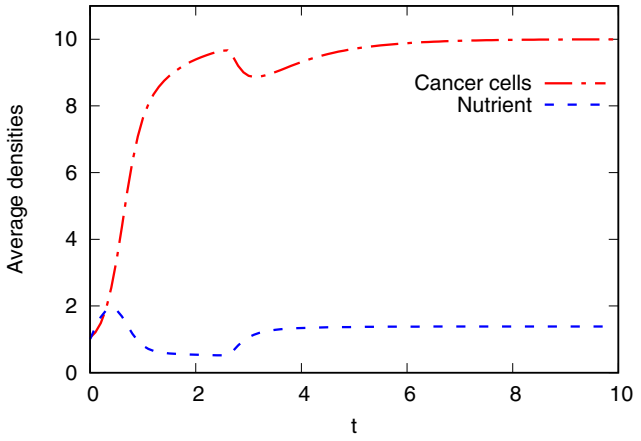

FIG. 2. The average cell density [see Eq. (10)] and the average nutrient density [see Eq. (11)], corresponding to the results in Fig. 1.

1. Results with homogeneous nutrient source

We assume initial conditions

$$\rho(\mathbf{r}, 0) = 1 + \gamma(\mathbf{r}),$$
$$n(\mathbf{r}, 0) = 1, \tag{23}$$

where $\gamma(\mathbf{r})$ is a small amplitude random variable and $\gamma(\mathbf{r}) \sim U(0, 1)$, where U is a uniform distribution. We set the dimensionless model parameters to be $c_1 = 1$, $\beta\varepsilon = 1$, $\tilde{\lambda}_n = 1$, and $\tilde{D} = 1$. We set the area of the domain in which the model is solved to be 25.6×25.6, with grid spacing $\Delta x = 0.1$ (smaller values were also tested, but this value is normally sufficiently small) and periodic boundary conditions on all sides. We set the nutrient source to be uniform $f(\mathbf{r}) = 1$, with amplitude $\tilde{S}_n = 10$.

In Fig. 1, the plots in the left-hand column are the density profile of the cells at a series of different times ($t = 2.6, 2.7, 2.8$, and 5), while the right-hand column displays plots of the local nutrient concentration. From the left column, it is clear that the total density of cells increases with time, as can also be seen in Fig. 2, where we plot the average cell density and nutrient density over the whole system as a function of time, which are defined in Eqs. (10) and (11). We see the peaks (i.e., locations of the centres of the cells) grow and split to fill the entire domain, due the fact that there is a source of nutrient everywhere, in contrast to the behavior seen, for example, in Fig. 3, where the source of nutrient is localized along the midline of the system. In Fig. 2 we see that initially the nutrient density increases, due to the low initial average cell density. Then, at $t \approx 0.5$, while the cell density increases, the nutrient density starts to decrease, due to the increased consumption. Over the time $2 \lesssim t \lesssim 3$ the peaks in the cells density distribution form. Consequently, the nutrient concentration then increases again at $t \approx 3$. After this, $\bar{n}(t)$ is roughly a constant ≈ 1.2, as shown in Fig. 2. The cell density continues to slowly increase to plateau at a constant value ≈ 10 at the time $t \approx 6$.

2. Results with inhomogeneous nutrient source

Figure 3 compares results for the cell density profile time evolution for three different values of $\tilde{D} = 1$, 10, and 100 (from left to right). For example, the results in the left-hand

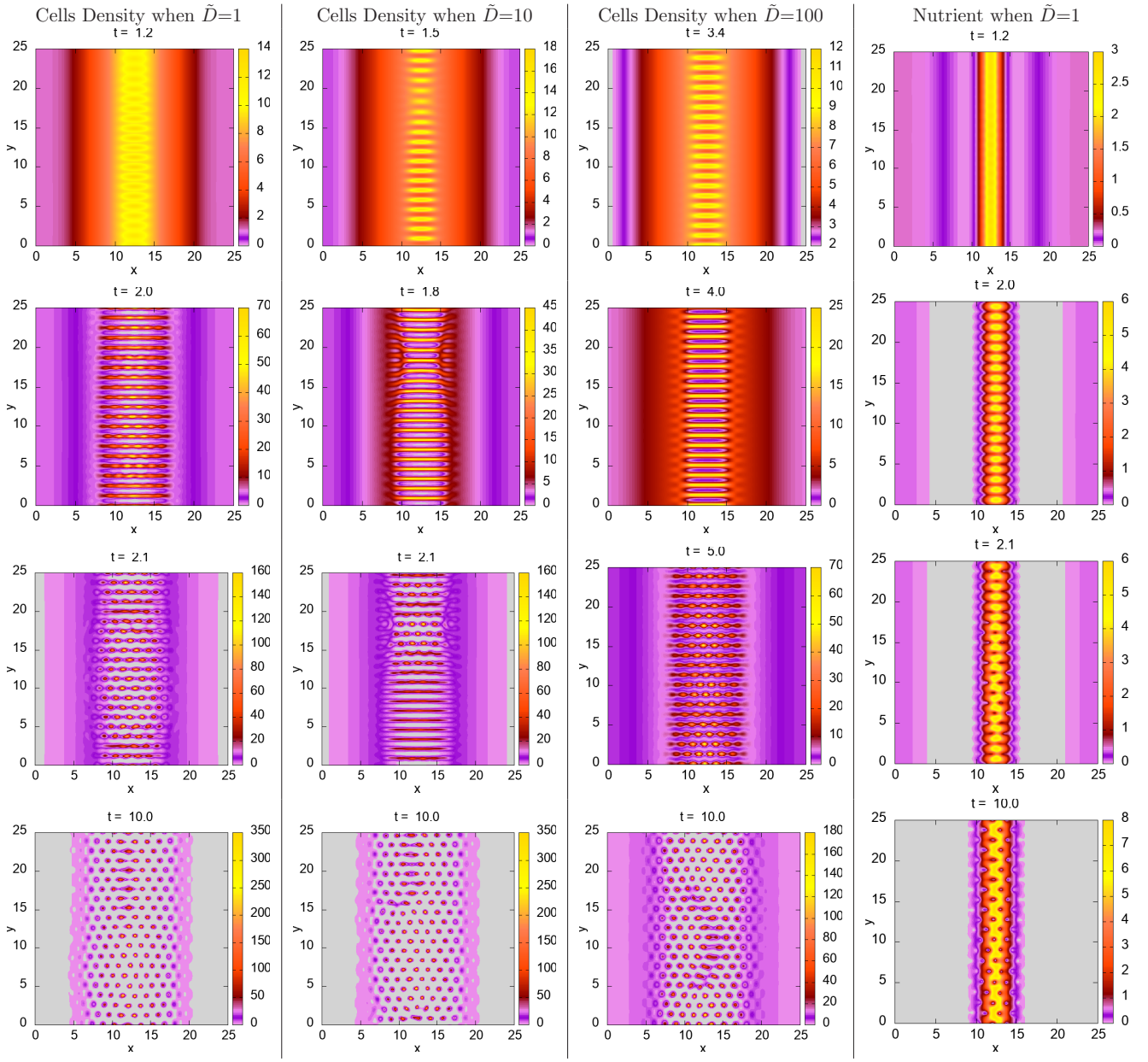

FIG. 3. The local density of the cells (left three columns, for $\tilde{D} = 1$, 10, and 100, from left to right) and the nutrient density for $\tilde{D} = 1$ (right hand column). The population growth constant $c_1 = 1$ and the energy scale in the interaction potential between cells $\beta\varepsilon = 1$. The nutrient source term has $\tilde{S}_n = 35$ with $f(\mathbf{r})$ given in Eq. (6) and nutrient uptake rate $\tilde{\lambda}_n = 1$. The area of the system is 25.6^2, with grid spacing $\Delta x = 0.05$.

column of Fig. 3 shows the evolution of cell density, displaying snapshots for the times $t = 1.2$, 2, 2.1, and 10. In these cases the nutrient source is located along the vertical mid line of the system [cf. Eq. (6)]. From an initial randomised distribution, the cell density grows in the vicinity of central nutrient source. When the density is sufficiently large, an instability (cf. Sec. II D) leads first to a striped pattern and then peaks. The density peaks (i.e., cells) are arranged in a roughly hexagonal pattern, which also impacts the nutrient distribution. The right hand column of Fig. 3 show the time evolution of the nutrient density for the case $\tilde{D} = 1$, corresponding to the left hand column cell density profiles.

In Fig. 4 we display plots of the total cell density and nutrient density calculated using Eqs. (10) and (11), corresponding to Fig. 3. These results are for three very different values of $\tilde{D} =$ 1, 10 and 100. Nonetheless, we see that in all three cases the results are all qualitatively rather similar, which demonstrates that for $\tilde{D} \gtrsim 1$ the results do not qualitatively depend on the precise value of $\tilde{D}$. Recall that in Sec. II D we note that the true value is $\tilde{D} \approx 10^6$ [see also the Appendix and Eq. (A5)], but also argue that we do not need to have such a large value. Owing to the qualitative similarity of the results shown in Fig. 3, we see that smaller values of $\tilde{D} \approx 10$ are acceptable.

The similarities for different values of the diffusion coefficient ratio $\tilde{D}$ can also be seen from the results in Fig. 4, whereby the steady value of $\bar{\rho} \approx 5$ and $\bar{n} \approx 0.5$ is reached by $t \approx 4$. Note that for the smaller $\tilde{D} = 1$ case there are small amplitude oscillations in both the cell and nutrient average

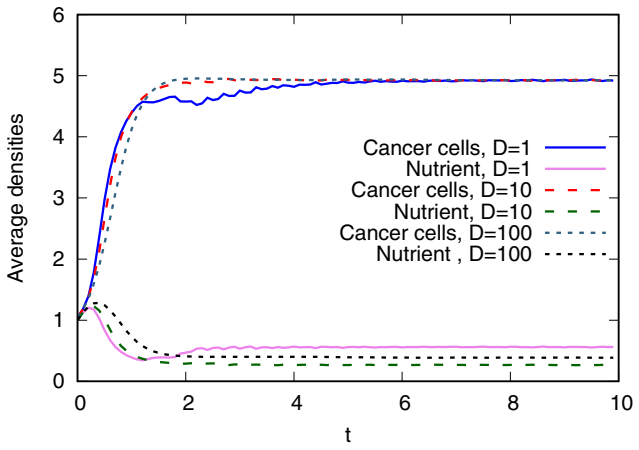

FIG. 4. The average cell density [see Eq. (10)] and the average nutrient density [see Eq. (11)], corresponding to the results in Fig. 3 when the diffusion coefficient $\tilde{D}$=1, 10, and 100, respectively.

densities for $t > 2$. These are due to new cells being formed and then dying in a periodic fashion.

By $t \approx 10$ the cell density profiles in Fig. 3 no longer change qualitatively, however, they are *not* stationary. We see that around the nutrient source along the line $x = L/2$, we have a region where the peaks grow and then split—modeling cell division—and then move away from the nutrient source, where they subsequently die due to the lack of nutrient away from the center line. In Fig. 5 we display a magnification of the cell density profile to highlight these mitotic events. The sequence of snapshots in Fig. 5 illustrates the cell splitting events that occurs between the times $t = 2.05$ and $t = 2.10$ with time increments of 0.01. We observe that a peak first elongates and then splits to form new peaks which remarkably mirrors a mitotic event. In the fourth row in Fig. 5, a peak spontaneously emerges between two existing ones, describing the average location of a new cell resulting from mitosis of one of the cells either side of it.

III. COMPETITION BETWEEN CANCER AND HEALTHY CELLS

In this section we extend the model presented in the previous section to include a second species of cells. Our aim is to study the competition between cancer cells and healthy cells. We denote the density of the cancerous and the healthy cells as ρ_1 and ρ_2, respectively. The generalization of Eqs. (5) and (9) is

$$\frac{\partial \rho_1(\mathbf{r},t)}{\partial t} = \Gamma_1 \nabla \cdot \left[\rho_1(\mathbf{r},t) \nabla \left(\frac{\delta \mathcal{F}[\rho_1,\rho_2]}{\delta \rho_1(\mathbf{r},t)} \right) \right] + [\lambda_{m1} n(\mathbf{r},t) - \lambda_{d1}] \rho_1(\mathbf{r},t), \tag{24}$$

$$\frac{\partial \rho_2(\mathbf{r},t)}{\partial t} = \Gamma_2 \nabla \cdot \left[\rho_2(\mathbf{r},t) \nabla \left(\frac{\delta \mathcal{F}[\rho_1,\rho_2]}{\delta \rho_2(\mathbf{r},t)} \right) \right] + [\lambda_{m2} n(\mathbf{r},t) - \lambda_{d2}] \rho_2(\mathbf{r},t), \tag{25}$$

$$\frac{\partial n(\mathbf{r},t)}{\partial t} = D_n \nabla^2 n(\mathbf{r},t) + S_n f(\mathbf{r}) - \lambda_{n1} \rho_1(\mathbf{r},t) n(\mathbf{r},t) - \lambda_{n2} \rho_2(\mathbf{r},t) n(\mathbf{r},t), \tag{26}$$

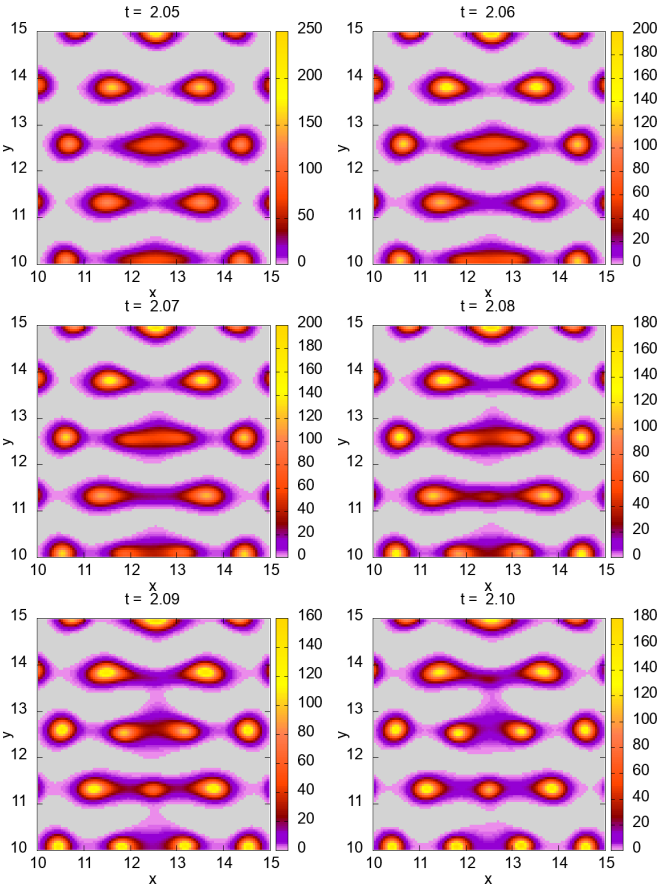

FIG. 5. Snapshots of several peak splitting events that occur between the times $t = 2.05$ and $t = 2.10$. The figures above are in time increments of 0.01 going from top left to bottom right, corresponding to the profiles plotted in the left hand column of Fig. 3, which are for $\tilde{D} = 1$.

where λ_{mi}, λ_{di}, λ_{ni}, and Γ_i have the same as their counterparts in Sec. II B for species i. The generalization of DDFT to describe a two component colloidal suspension was discussed in Ref. [65]. The above reduces to this DDFT if the BD terms are set to zero.

For such a binary system we may approximate the intrinsic Helmholtz free energy of the system as in Refs. [43,65], namely,

$$\mathcal{F}[\{\rho_i(\mathbf{r},t)\}] = k_B T \sum_{i=1}^{2} \int d\mathbf{r} \rho_i(\mathbf{r},t) \left\{ \ln \left[\Lambda_i^d \rho_i(\mathbf{r},t) \right] - 1 \right\} + \frac{1}{2} \sum_{i,j=1}^{2} \int d\mathbf{r} \int d\mathbf{r}' \rho_i(\mathbf{r},t) \rho_j(\mathbf{r}',t) V_{ij}(|\mathbf{r}-\mathbf{r}'|), \tag{27}$$

where V_{ij} are the pair interactions potentials, discussed further below and Λ_i are the thermal de Broglie wavelengths for species i. The indices i, $j = 1, 2$ label the two different species of particles (healthy and cancer); we assign 1 for cancer cells and 2 for healthy cells. Substituting Eq. (27) into Eqs. (24)

and (25), we obtain

$$\frac{\partial\rho_1(\mathbf{r},t)}{\partial t} = \nabla\cdot\Bigg(\Gamma_1\rho_1(\mathbf{r},t)\nabla\Bigg\{k_BT\ln\left[\Lambda_1^d\rho_1(\mathbf{r},t)\right] + \int d\mathbf{r}'\rho_1(\mathbf{r}',t)V_{11}(|\mathbf{r}-\mathbf{r}'|) + \int d\mathbf{r}'\rho_2(\mathbf{r}',t)V_{12}(|\mathbf{r}-\mathbf{r}'|)\Bigg\}\Bigg) + [\lambda_{m1}n(\mathbf{r},t)-\lambda_{d1}]\rho_1(\mathbf{r},t) \tag{28}$$

and

$$\frac{\partial\rho_2(\mathbf{r},t)}{\partial t} = \nabla\cdot\Bigg(\Gamma_2\rho_2(\mathbf{r},t)\nabla\Bigg\{k_BT\ln\left[\Lambda_2^d\rho_2(\mathbf{r},t)\right] + \int d\mathbf{r}'\rho_1(\mathbf{r}',t)V_{21}(|\mathbf{r}-\mathbf{r}'|) + \int d\mathbf{r}'\rho_2(\mathbf{r}',t)V_{22}(|\mathbf{r}-\mathbf{r}'|)\Bigg\}\Bigg) + [\lambda_{m2}n(\mathbf{r},t)-\lambda_{d2}]\rho_2(\mathbf{r},t). \tag{29}$$

As in Sec. II we model the cell-cell interactions via soft, purely repulsive, and radially symmetric pair potentials given by

$$V_{ij}(r) = \varepsilon_{ij}e^{-(r/R_{ij})^4}, \tag{30}$$

where the parameters ε_{ij} specify the strength of the repulsion between pairs of cells of species i and j and R_{ij} define the range of the interactions. Thus, we choose $R_{11} \geqslant R_{22}$, modelling cancer cells that are the same size or slightly larger than the healthy cells, and we choose $\varepsilon_{12} > \varepsilon_{11} = \varepsilon_{22}$, so that peaks of the different species do not occur at the same point in space. In some cases, we choose $R_{12} = \frac{1}{2}(R_{11}+R_{22})$, but we also consider cases where $R_{12} > \frac{1}{2}(R_{11}+R_{22})$ since this promotes demixing of the two cell species and also $R_{12} < \frac{1}{2}(R_{11}+R_{22})$, which promotes penetration of the cancer cells in between the healthy cells [43,52,65].

A. Nondimensionalization

We nondimensionlize the system of integropartial differential equations given in Eqs. (28), (29), and (26) in a manner similar to previously, using $t = \frac{R_{11}^2 t^*}{D_c}$, $x = \frac{x^*}{R_{11}}$, $y = \frac{y^*}{R_{11}}$, $\rho_1 = \frac{\rho_1^*}{R_{11}^2}$, $\rho_2 = \frac{\rho_2^*}{R_{11}^2}$, $n = \frac{\lambda_{d1}n^*}{\lambda_{m1}}$, and $V_{ij}(r/R_{11}) = \varepsilon_{ij}\tilde{V}_{ij}(r^*)$, where the asterisked quantities are dimensionless and $D_c = \Gamma_1 k_BT$. Here, the scaling on space is based on the range of the interaction between two cancer cells, R_{11}. Defining the dimensionless parameters [cf. Eq. (13)],

$$c_1 = \frac{R_{11}^2\lambda_{d1}}{D_c}, \quad c_2 = \frac{R_{11}^2\lambda_{m2}\lambda_{d1}}{D_c\lambda_{m1}}, \quad \alpha = \frac{\lambda_{d2}\lambda_{m1}}{\lambda_{d1}\lambda_{m2}},$$
$$\tilde{D}_2 = \frac{\Gamma_2}{\Gamma_1}, \quad \tilde{D}_n = \frac{D_n}{D_c}, \quad \tilde{S}_n = \frac{R_{11}^2 S_n\lambda_{m1}}{\lambda_{d1}D_c},$$
$$\tilde{\lambda}_{n1} = \frac{\lambda_{n1}}{D_c}, \quad \tilde{\lambda}_{n2} = \frac{\lambda_{n2}}{D_c},$$

noting that $\tilde{D}_2$ is the ratio of the diffusion coefficients of healthy cells to cancer cells. We get

$$\frac{\partial\rho_1(\mathbf{r},t)}{\partial t} = \nabla^2\rho_1(\mathbf{r},t) + \nabla\cdot\left[\rho_1(\mathbf{r},t)\nabla\int d\mathbf{r}'\rho_1(\mathbf{r}',t)\beta\varepsilon_{11}\tilde{V}_{11}(|\mathbf{r}-\mathbf{r}'|)\right] + \nabla\cdot\left[\rho_1(\mathbf{r},t)\nabla\int d\mathbf{r}'\rho_2(\mathbf{r}',t)\beta\varepsilon_{12}\tilde{V}_{12}(|\mathbf{r}-\mathbf{r}'|)\right] + c_1[n(\mathbf{r},t)-1]\rho_1(\mathbf{r},t), \tag{31}$$

$$\frac{\partial\rho_2(\mathbf{r},t)}{\partial t} = \tilde{D}_2\nabla^2\rho_2(\mathbf{r},t) + \nabla\cdot\left[\rho_2(\mathbf{r},t)\nabla\int d\mathbf{r}'\rho_1(\mathbf{r}',t)\beta\varepsilon_{21}\tilde{V}_{21}(|\mathbf{r}-\mathbf{r}'|)\right] + \nabla\cdot\left[\rho_2(\mathbf{r},t)\nabla\int d\mathbf{r}'\rho_2(\mathbf{r}',t)\beta\varepsilon_{22}\tilde{V}_{22}(|\mathbf{r}-\mathbf{r}'|)\right] + c_2[n(\mathbf{r},t)-\alpha]\rho_2(\mathbf{r},t), \tag{32}$$

$$\frac{\partial n(\mathbf{r},t)}{\partial t} = \tilde{D}_n\nabla^2 n(\mathbf{r},t) + \tilde{S}_n f(\mathbf{r}) - \tilde{\lambda}_{n1}\rho_1(\mathbf{r},t)n(\mathbf{r},t) - \tilde{\lambda}_{n2}\rho_2(\mathbf{r},t)n(\mathbf{r},t). \tag{33}$$

Where the asterisks have been dropped for clarity.

B. Parameters values

For both the healthy and cancer cell growth rate parameters, diffusion coefficients, and the parameters relating to the nutrient dynamics we use the same values that are argued for in the Appendix. The main change is to make the growth rate parameters for the cancer cells larger than those of the healthy cells in order for them to reproduce and grow faster (or die slower) than the healthy cells. The parameter values are summarised in Table III and the corresponding dimensionless parameter values are given in Table IV. The other main addition to the model for both healthy and cancer cells that must be considered are the parameter values in the interaction potential between the different types of cells, given in Eq. (7). The parameter values we choose are given in Table III. These values are chosen to (i) make the cancer cells either the same size or slightly larger than the healthy cells [66] and (ii) to make sure the cancer cells do not overlap with the healthy cells.

C. Linear stability analysis for two species model

The governing equations for the time evolution of the density profile of the cancer cells, the healthy cells and the nutrient are given by Eqs. (31)–(33). We note for $\alpha \neq 1$ there is no spatially uniform positive steady state to this system. We consider here the linear stability of uniform state $\rho_1 = \rho_1^b > 0$ and $\rho_2 = \rho_2^b > 0$ for the case $c_1, c_2 \ll \xi \ll 1$, where ξ is the amplitude of the density perturbation; the small magnitude of c_1 and c_2 in comparison to the other parameters is evident from Table IV. In setting $c_1 = c_2 = 0$ for the purposes of the linear stability analysis, we are assuming the growth of cells occurs on a much longer timescale than that of the cell motion. This assumption means that the nutrient Eq. (33) decouples from Eqs. (31) and (32), so that in what follows, stability of a uniform state is predominantly governed by cell density and the cell-cell interaction process.

TABLE III. Model parameters and their units. Values marked with asterisk (*) are estimates from Secs. IIIV and III B.

Symbol	Typical value	Unit	Source
$\rho_1(\mathbf{r},t)$	$3\times10^{5*}$	cm^{-2}	Estimated
$\rho_2(\mathbf{r},t)$	$3\times10^{5*}$	cm^{-2}	Estimated
$n(\mathbf{r},t)$	3^*	mg/L	Estimated
$V_{11}(r)$	ε_{11}	Joule	Estimated
$V_{12}(r)$	ε_{12}	Joule	Estimated
$V_{22}(r)$	ε_{22}	Joule	Estimated
R_{11}	0.001	cm	[61]
R_{22}	0.0009	cm	[61]
λ_{m1}	0.00015^*	$\mathrm{L\,min^{-1}mg^{-1}}$	Estimated
λ_{m2}	0.000015^*	$\mathrm{L\,min^{-1}mg^{-1}}$	Estimated
λ_{d1}	0.00005^*	min^{-1}	Estimated
λ_{d2}	0.000005^*	min^{-1}	Estimated
λ_{n1}	3^*	min^{-1}	Estimated
λ_{n2}	3^*	min^{-1}	Estimated
D_c	$1.3\times10^{-9*}$	$\mathrm{cm^2\,min^{-1}}$	Estimated
D_h	$1.1\times10^{-9*}$	$\mathrm{cm^2\,min^{-1}}$	Estimated
D_n	0.0012	$\mathrm{cm^2min^{-1}}$	[9]
Γ_1	3×10^{10}	$\mathrm{min\,g^{-1}}$	Sec. IIIA
Γ_2	2.5×10^{10}	$\mathrm{min\,g^{-1}}$	Sec. IIIA
T	310	K	[61]
k_B	1.38×10^{-23}	Joule/K	[62]
ε_{11}	$1k_BT$	Joule	Estimated
ε_{12}	$1.5k_BT$	Joule	Estimated
ε_{22}	$1k_BT$	Joule	Estimated
ρ_0	3×10^5	cm^{-2}	Table I
L^2	6×10^{-4}	cm^2	Table I
S_n	433^*	$\mathrm{mg\,L^{-1}min^{-1}cm^{-2}}$	Estimated

We assume the cell density perturbations are of the form

$$\begin{aligned}\rho_1(\mathbf{r},t) &= \rho_1^b + \delta\rho(\mathbf{r},t)\\ &= \rho_1^b + \xi e^{i(\mathbf{k}\cdot\mathbf{r})+\omega t},\end{aligned} \tag{34}$$

and

$$\begin{aligned}\rho_2(\mathbf{r},t) &= \rho_2^b + \chi\delta\rho(\mathbf{r},t)\\ &= \rho_2^b + \chi\xi e^{i(\mathbf{k}\cdot\mathbf{r})+\omega t},\end{aligned} \tag{35}$$

TABLE IV. Dimensionless parameter values of the model. $\gamma(\mathbf{r})$ is given in Eq. (23).

Nondimensional p	Dimensional form	Value	Used value
ρ_1^*	$\rho_1/\hat{\rho}_1$	1	$6+\gamma(\mathbf{r})^*$
ρ_2^*	$\rho_2/\hat{\rho}_2$	1	$6+\gamma(\mathbf{r})^*$
n^*	$n/\hat{n}$	3	3
c_1	$R_{11}^2\lambda_{d1}/D_c$	0.038	0.5, 0.6
c_2	$R_{11}^2\lambda_{m2}\lambda_{d1}/D_c\lambda_{m1}$	0.0038	0.5, 0.6
α	$\lambda_{d2}\lambda_{m1}/\lambda_{d1}\lambda_{m2}$	1	2
$\tilde{D}_2$	D_h/D_c	1.1	1
$\tilde{D}_n$	D_n/D_c	10^6	1
$\tilde{S}_n$	$R_{11}^2S_n\lambda_{m1}/\lambda_{d1}D_c$	10^6	8, 9
$\tilde{\lambda}_{n1}$	λ_{n1}/D_c	10^6	1
$\tilde{\lambda}_{n2}$	λ_{n2}/D_c	10^6	1
$\varepsilon_{11}\tilde{V}_{11}(r^*)$	$V_{11}(r/R_{11})$	See Eq. (7)	–
$\varepsilon_{12}\tilde{V}_{12}(r^*)$	$V_{12}(r/R_{11})$	See Eq. (7)	–
$\varepsilon_{22}\tilde{V}_{22}(r^*)$	$V_{22}(r/R_{11})$	See Eq. (7)	–

where $0<\xi\ll1$, k is the wave number, χ is the ratio between the amplitude of the modulation in the two components, and the growth or decay rate is determined by the dispersion relation $\omega=\omega(k)$, where $k=|\mathbf{k}|$. Substituting Eqs. (34) and (35) into Eqs. (31) and (32), on linearizing in ξ we obtain [60]

$$\omega(k)\begin{pmatrix}1\\ \chi\end{pmatrix} = \mathbf{M}\begin{pmatrix}1\\ \chi\end{pmatrix}, \tag{36}$$

where the matrix

$$\mathbf{M} = -k^2\begin{pmatrix}1+\rho_1^b\beta\varepsilon_{11}\hat{V}_{11}(k) & \rho_2^b\beta\varepsilon_{12}\hat{V}_{12}(k)\\ \rho_1^b\beta\varepsilon_{21}\hat{V}_{21}(k) & 1+\rho_2^b\beta\varepsilon_{22}\hat{V}_{22}(k)\end{pmatrix}. \tag{37}$$

We can rewrite the matrix $\mathbf{M}$ as a product of two matrices $\mathbf{M}=\mathbf{N}\cdot\mathbf{E}$, where

$$\mathbf{N} = \begin{pmatrix}-\rho_1^bk^2 & 0\\ 0 & -\rho_2^bk^2\end{pmatrix}, \tag{38}$$

and

$$\mathbf{E} = \begin{pmatrix}\left[\frac{1}{\rho_1^b}+\beta\varepsilon_{11}\hat{V}_{11}(k)\right] & \beta\varepsilon_{12}\hat{V}_{12}(k)\\ \beta\varepsilon_{21}\hat{V}_{21}(k) & \left[\frac{1}{\rho_2^b}+\beta\varepsilon_{22}\hat{V}_{22}(k)\right]\end{pmatrix}. \tag{39}$$

We can now determine the dispersion relation $\omega(k)$ by calculating the eigenvalues of $\mathbf{N}\cdot\mathbf{E}$,

$$\omega(k) = \frac{\mathrm{Tr}(\mathbf{N}\cdot\mathbf{E})}{2} \pm \sqrt{\frac{\mathrm{Tr}(\mathbf{N}\cdot\mathbf{E})^2}{4} - |\mathbf{N}\cdot\mathbf{E}|}, \tag{40}$$

where $|\mathbf{N}\cdot\mathbf{E}|$ denotes the determinant of the matrix $\mathbf{N}\cdot\mathbf{E}$ [60]. When $\omega(k)<0$ for all wave numbers k, the system is linearly stable. If, however, $\omega(k)>0$ for any wave number k, then the uniform density state is linearly unstable. Since $\mathbf{N}$ is a (negative definite) diagonal matrix its inverse $\mathbf{N}^{-1}$ exists for all nonzero densities and temperatures, enabling us to write Eq. (36) as the generalized eigenvalue problem

$$(\mathbf{E}-\mathbf{N}^{-1}\omega)\hat{\chi} = 0, \tag{41}$$

where $\hat{\chi}=(1,\chi)$. As $\mathbf{E}$ is a symmetric matrix, all eigenvalues are real. It follows that the linear stability threshold is determined by $|\mathbf{E}|=0$, i.e., by the condition

$$\begin{aligned}D(k) \equiv &\left[1+\rho_1^b\beta\varepsilon_{11}\hat{V}_{11}(k)\right]\left[1+\rho_2^b\beta\varepsilon_{22}\hat{V}_{22}(k)\right]\\ &-\rho_1^b\rho_2^b\beta^2\varepsilon_{12}^2\hat{V}_{12}^2(k) = 0.\end{aligned} \tag{42}$$

In Fig. 6 we display the linear stability threshold for different values of the concentration $\phi\equiv\rho_1^b/\rho$, where $\rho\equiv\rho_1^b+\rho_2^b$ is the total density and ρ_1^b, ρ_2^b are the densities of cancer and healthy cells, respectively. For state points above the linear stability threshold lines in Fig. 6 the system forms peaks, modeling the distribution of the cells. The instability line is obtained by tracing the locus defined by $D(k_c)=0$ and $D'(k_c)=0$, where $D(k)$ is given in Eq. (42) and $k_c\neq0$ is the wave number at the minimum of $D(k)$ [i.e., $D(k=k_c)=0$]. Note that as the cell radii ratio R_{22}/R_{11} is increased (or, of course, decreased), the two wave numbers at which the system can become linearly unstable, $k_c\approx2\pi/R_{11}$ or $k_c\approx2\pi/R_{22}$, move apart leading to the linear stability threshold developing a cusp, as shown by the "corners" in some of the curves in the lower figure of Fig. 6. The cusp appears when the two minima in $D(k)$ both satisfy $D(k_c)=0$ and can be

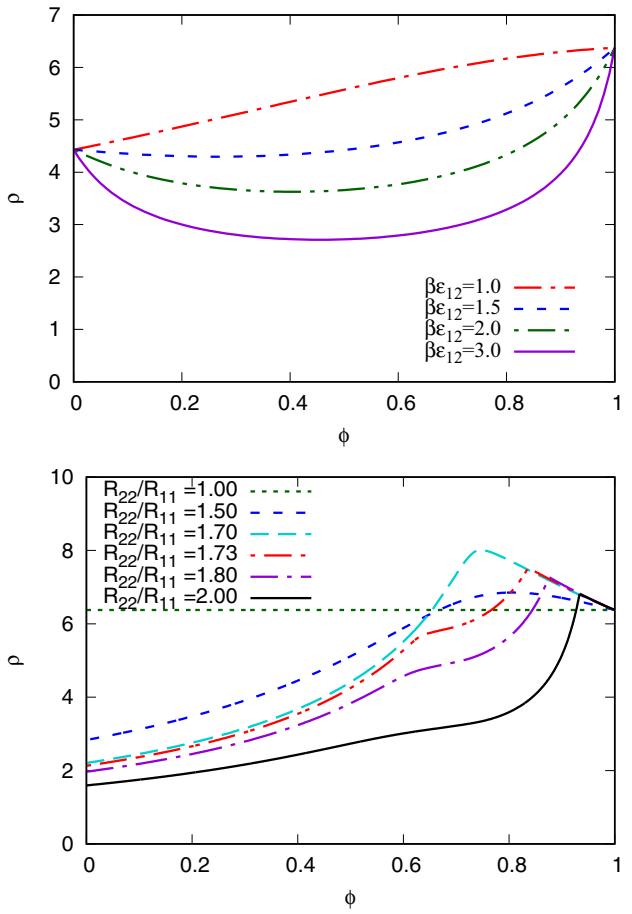

FIG. 6. The linear stability threshold for the two species cells [see Eqs. (31) and (32)] plotted in the total density $\rho \equiv \rho_1^b + \rho_2^b$ versus concentration $\phi \equiv \rho_1^b/\rho$ plane. The uniform density state is linearly unstable above this line. The top plot shows the curves for $R_{11} = 1$, $R_{22} = 1.2$, $R_{12} = 1.1$, $\beta\varepsilon_{11} = \beta\varepsilon_{22} = 1$ and for varying $\beta\varepsilon_{12}$, as given in the key. The curves in the lower plot are for varying $R_{22} = 1$, 1.5, 1.7, 1.73, 1.8, and 2. We set the cross-interaction radius $R_{12} = \frac{1}{2}(R_{11} + R_{22})$ and $\beta\varepsilon_{11} = \beta\varepsilon_{12} = \beta\varepsilon_{22} = 1$.

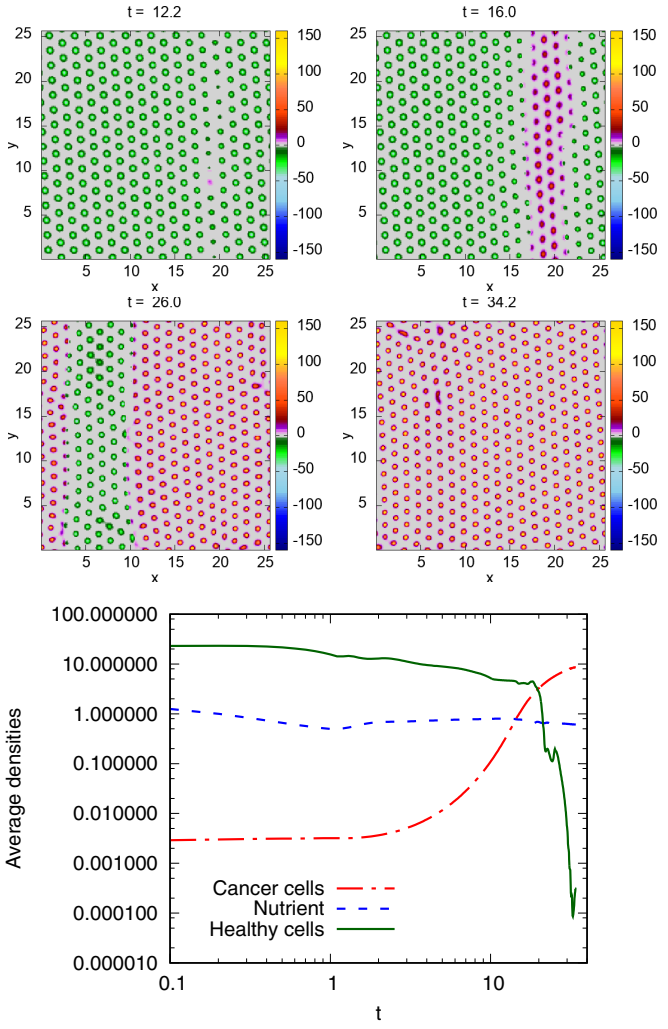

FIG. 7. Top four panels: plots of $(\rho_1 - \rho_2)$, the density profile of the cancer cells minus the density of the healthy cells, at times $t = 0.1$, 16, 26, and 34.2. The nutrient uptake rates $\tilde{\lambda}_{n1}$=1 and $\tilde{\lambda}_{n2}$=1, the population growth constants $c_1 = c_2 = 0.5$, and the threshold nutrient concentration for healthy cells $\alpha = 2$. The nutrient source is homogeneous, with $f(\mathbf{r}) = 1$ and $\tilde{S}_n = 9$. The area of the domain is 25.6×25.6 and $\Delta x = \Delta y = 0.1$. The cell-cell pair interaction potential parameters are $\beta\varepsilon_{11}$=1, $\beta\varepsilon_{12}$=1.5, $\beta\varepsilon_{11}$=1, $R_{11} = R_{22} = 1$, and $R_{12} = 0.9$. Bottom: the corresponding average cell density [see Eq. (10)] and the average nutrient density [see Eq. (11)].

determined by simultaneously solving the system of algebraic equations $D(k_c) = D'(k_c) = D''(k_c) = D'''(k_c) = 0$. We find that on increasing R_{22}/R_{11} the cusp appears at $R_{22}/R_{11} = 1.73$, $\rho = 8.26$, and $\phi = 0.74$ (red curve in the bottom plot) and is present for $R_{22}/R_{11} > 1.73$.

D. Numerical results

In this section we discuss some representative results showing the competition between healthy and cancer cells, obtained by solving numerically the system of integro-partial differential Eqs. (31)–(33) using the numerical methods discussed in Sec. II E. We investigate the evolution of the cells starting from various different initial arrangements and the effect of the cross-species interaction range R_{12}.

1. Spread from a few cancer cells within healthy tissue

To model the growth and spread of a tumor within healthy tissue we consider a case where we first initiate the system with one half containing predominantly healthy tissue, the other half containing cancerous tissue (with uniform densities in each half), and a uniform nutrient density. As the system evolves, peaks form in the two cell density profiles and over time the cancer cells displace the healthy cells till the total average density of healthy cells is small. We then stop the simulation and *swap* the labels on the two density profiles, so that the (more realistic) initial condition for the following simulation consists of an array of peaks (cells) in the healthy cell density profile and a low density of cancer cells; i.e., for the initial conditions we define $\rho_1(\mathbf{r}, t = 0) = \rho_2^{\ddagger}(\mathbf{r}, t = 20)$ and $\rho_2(\mathbf{r}, t = 0) = \rho_1^{\ddagger}(\mathbf{r}, t = 20)$, where $\rho_1^{\ddagger}(\mathbf{r}, t = 20)$ and $\rho_2^{\ddagger}(\mathbf{r}, t = 20)$ are the final profiles at time $t = 20$ from the preliminary simulation.

Snapshots from the subsequent evolution are displayed in Fig. 7. These results are for the population growth constants $c_1 = c_2 = 0.5$ and the threshold nutrient concentration for healthy cells $\alpha = 2$. We fix the various cell-cell interaction parameters to be $\beta\varepsilon_{11} = \beta\varepsilon_{22} = 1$, $\beta\varepsilon_{12} = 1.5$ (so that density peaks of the two different cell types do not overlap), $R_{11} = R_{22} = 1$ and $R_{12} = 0.9$. The nutrient uptake rate for cancer cells $\tilde{\lambda}_{n1} = 1$ and for healthy cells $\tilde{\lambda}_{n2} = 1$. The area of the domain in which the model is solved is 25.6×25.6 and the nutrient source is uniform, with $f(\mathbf{r}) = 1$ and $\tilde{S}_n = 9$. The diffusion coefficients for both cell species are equal, $\tilde{D}_c = \tilde{D}_h = 1$.

In Fig. 7 we plot the difference between the density profiles $(\rho_1 - \rho_2)$. Positive values in this quantity correspond to regions where the cancer cells are present (where the peaks are purple-red, with yellow maxima) and negative values where the healthy cells are present (where the peaks are green). In regions that are gray, both densities are low. The Fig. 7 profiles are snapshots at the times t=12.2, 16, 26, and 34.2. At t=12.2 the first cancer cell becomes visible. As time increases, the cancer cells proliferate to form a vertical strip of cancerous tissue, shown in the top right pannel. The fact that it is a vertical strip is due to the original initial conditions. By the time $t = 26$ the cancer cells have invaded two thirds of the healthy area and by $t = 34.2$ they cover the entire domain, having displaced all the healthy cells.

In the bottom panel of Fig. 7, we plot the average densities of the two species of cells and also of the nutrients, calculated using the two component generalisation of Eqs. (10) and (11), respectively. We see that over time the average nutrient density is roughly constant, but the density of the healthy cells decreases over time, while the average density of the cancer cells increases. Interestingly, the average density of the healthy cells does not decrease monotonically; there are instances where there are brief increases, where healthy cells momentarily find gaps around the evolving cancer into which they try and grow. However, the overall trend is for the healthy cells to be displaced and die out.

2. *Growth of a cancer that is initially small and circular*

Figures 8–12 display results for the evolution over time starting from the initial condition

$$\rho_1(\mathbf{r}, 0) = \begin{cases} 6 + \gamma(\mathbf{r}) & (x - 12.8)^2 + (y - 12.8)^2 \leqslant 6^2 \\ 0 & (x - 12.8)^2 + (y - 12.8)^2 > 6^2 \end{cases}, \tag{43}$$

$$\rho_2(\mathbf{r}, 0) = \begin{cases} 0 & (x - 12.8)^2 + (y - 12.8)^2 \leqslant 6^2 \\ 6 + \gamma(\mathbf{r}) & (x - 12.8)^2 + (y - 12.8)^2 > 6^2 \end{cases}, \tag{44}$$

and $n(\mathbf{r}, 0) = 0.5$, where $\gamma(\mathbf{r})$ is a random variable drawn from a uniform distribution on the interval (0,1). This initial condition corresponds to a small circular cancer of radius 6 in the middle of the healthy cells. Figures 8–10 show simulations with $R_{12} = 0.9$, 1, 1.1, respectively, with all other parameters fixed as in Fig. 7, noting that $R_{11} = R_{22} = 1$. In the case of $R_{12} = 0.9$, the two cell types can tolerate being closer to each other thereby promoting mixing behavior; this despite the repulsive strength across types, $\beta\varepsilon_{12} = 1.5$, being stronger than that between them $\beta\varepsilon_{11} = \beta\varepsilon_{22} = 1$. For $R_{12} = 1.1$, we expect more demixing type behavior.

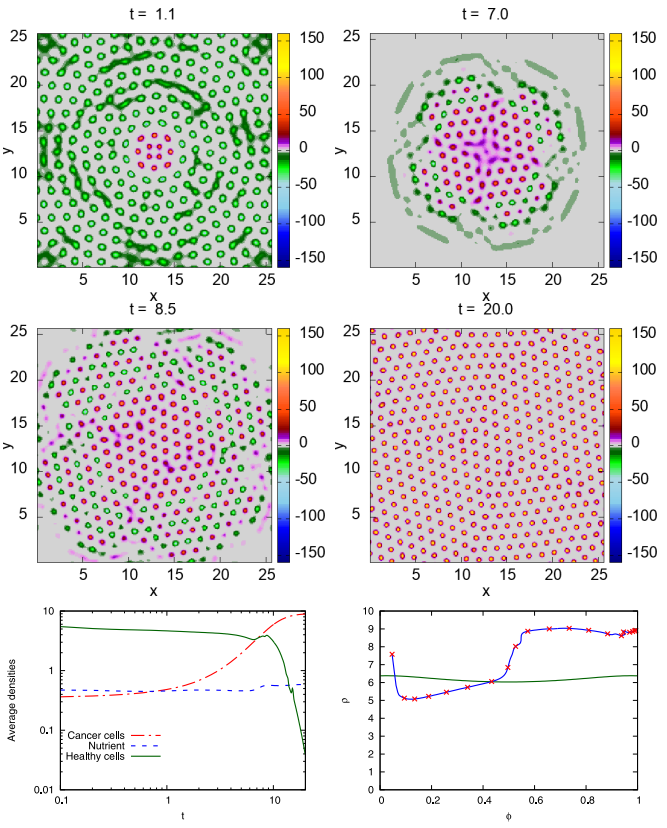

FIG. 8. Snapshots of $(\rho_1 - \rho_2)$, the density profile of the cancer cells minus that of the healthy cells, at the times $t = 0.1$, 6.5, 10, and 20 evolving from the initial conditions defined in Eqs. (43) and (44). The system parameters are $\tilde{\lambda}_{n1} = \tilde{\lambda}_{n2} = 1$, $\tilde{D}_c = \tilde{D}_2 = 1$, $c_1 = c_2 = 0.5$, and $\alpha = 2$. The nutrient source is homogeneous with $f(\mathbf{r}) = 1$ and $\tilde{S}_n = 9$. The area of the domain is 25.6×25.6 and $\Delta x = \Delta y = 0.1$. The parameters in the pair interaction potentials between the cells are $\beta\varepsilon_{11} = 1$, $\beta\varepsilon_{12} = 1.5$, $\beta\varepsilon_{11} = 1$, $R_{11} = R_{22} = 1$, and $R_{12} = 0.9$. In the bottom left panel are plotted the corresponding average cell densities [see Eq. (10)] and the average nutrient density [see Eq. (11)]. In the bottom right panel we plot the trajectory of the time evolution in the (ρ, ϕ) plane. Note that the points on this trajectory correspond to the integer times $t = 0, 1, 2, \ldots$. We also plot the linear stability threshold for this system. When the trajectory dips below this line, the system temporarily "melts."

We see in Fig. 8 that although within the domains where the different cell species are initiated—see Eqs. (43) and (44)—the densities are uniform, i.e., liquidlike, rather than a "crystalline" state with density peaks, the peaks corresponding to the locations of the cells rapidly form and are already present by the time $t = 0.1$. However, this sudden initial growth leads to a drop in the nutrient level, as can be seen at $t \approx 5$ in Fig. 8. The drop in nutrient level then leads to a drop in the overall number of healthy cells, which leads to the "crystal" melting temporarily, which corresponds to the cells being distributed in disordered liquid-like configurations; biologically, this melting phenomenon can be viewed as a temporary state of flux, whereby cells are moving around relatively rapidly and the densities shown are the average density distribution of the cell centres. The nutrient level then recovers and the system "refreezes" and over time the cancer cells penetrate the healthy tissue and eventually the healthy cells all die out.

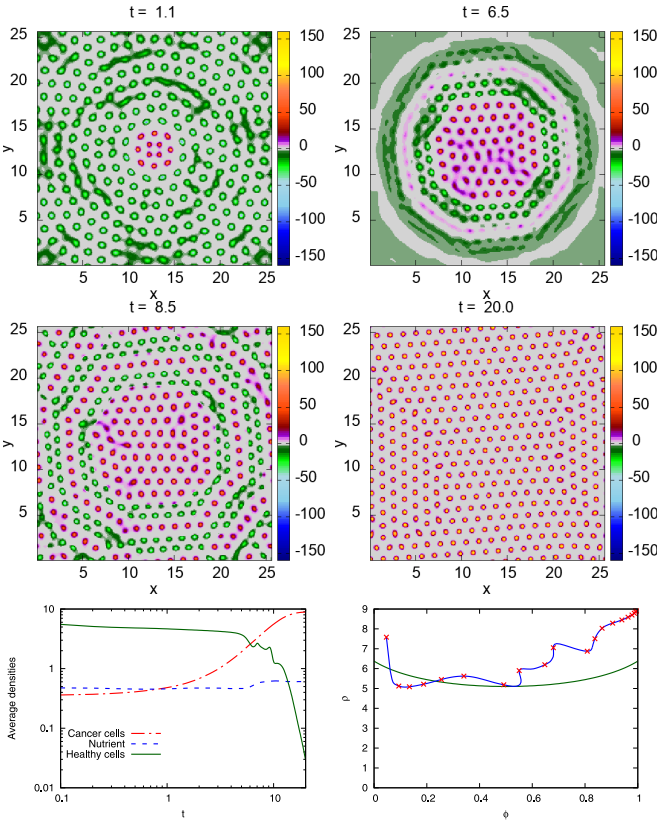

FIG. 9. Snapshots of $(\rho_1 - \rho_2)$ at the times $t = 1.1$, 6.5, 8.5, and 20. All the parameters here are the same as those in Fig. 8, except here the cross interaction pair potential radius is $R_{12} = 1$, which is slightly larger.

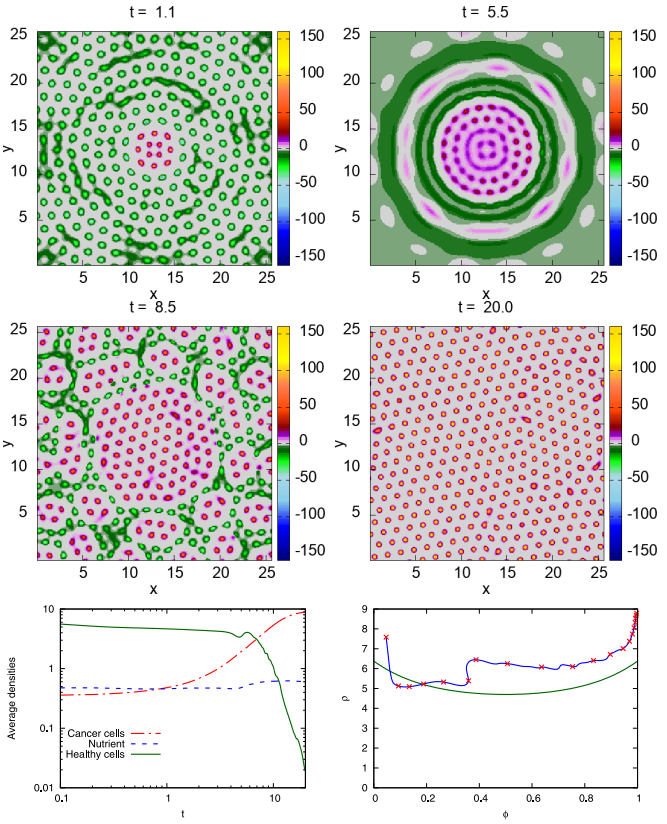

FIG. 10. Snapshots of $(\rho_1 - \rho_2)$ at the times $t = 1.1$, 5.5, 8.5, and 20. All the parameters here are the same as those in Figs. 8 and 9, except here the cross interaction pair potential radius is even larger, $R_{12} = 1.1$.

The temporary "melting" can be understood if one plots the trajectory of the system in the total density versus concentration (ρ, ϕ) plane, in addition to plotting the threshold for the system to be linearly unstable, given by Eq. (42). This is displayed in the bottom right panel of Fig. 8. Recall that above the stability line the system is linearly unstable and forms peaks. We see that when the trajectory dips below this line is when the system temporarily "melts."

In the Fig. 9 we plot results for the case when all the model parameters are the same as those in the previous case (that displayed in Fig. 8), except now the radius in the cross interaction pair potential $R_{12} = 1$, which is slightly larger (for the results in Fig. 8 we have $R_{12} = 0.9$). In Fig. 9 we plot $(\rho_1 - \rho_2)$ at the times t=0.1, 5.5, 9, and 20. As before, we see that the total density of the cancer cells increase with the time and the healthy cells retreat from the center and finally all the healthy cells die by the time $t = 20$. The consequence of the increased value of R_{12} is that there is now a tendency for the cancer cells to penetrate into layers beyond the initial interfacial layer of healthy cells, and so form alternating layers of healthy and cancerous cells—see, e.g., the plot for the time $t = 7.5$. The averages densities over time are shown in the bottom left panel of the Fig. 9 and in the bottom right is the trajectory in the (ρ, ϕ) plane and also the corresponding linear stability threshold line.

In Fig. 10 we present results for an even larger value of the cross interaction radius, $R_{12} = 1.1$. Comparing with Figs. 8 and 9, we see that the effect of this increase is to further increase the tendency of the cancer cells to penetrate into the healthy tissue (metastasis) and in this case forming roughly circular clumps of cancer cells ahead of the main tumor, rather than layers.

The dynamics shown in each of Figs. 8–10 reflects metastasis. Smaller cross species interaction range, R_{12}, lead to a disordered infiltration of healthy tissue by individual tumor cells, which is more ordered for $R_{12} = 1$. For the larger R_{12}, tumor cells appears to infiltrate healthy tissue as small clusters. In each case, much of the initial mixing of cell types occurs during the transient melting phase, the timescale for which decreases on increasing R_{12} (as can be seen from linear stability threshold diagrams for each of the plots); we note, however, the central core structure of tumor cells is maintained during the melting phase. The different manner of infiltration is an interesting consequence of the modeling assumptions, but it would be experimentally challenging to discern which of these patterns, if any, are relevant biologically.

3. The effect of varying $\beta\varepsilon_{12}$

Guided by the results in Fig. 6, we now investigate the effect on the cancer development of varying the cross-species repulsion strength, $\beta\varepsilon_{12}$. In Fig. 11 we display results for three different values, $\beta\varepsilon_{12} = 1$, 1.75, and 2. We see that the speed of the cancer cells to penetrate the healthy tissue increases as we

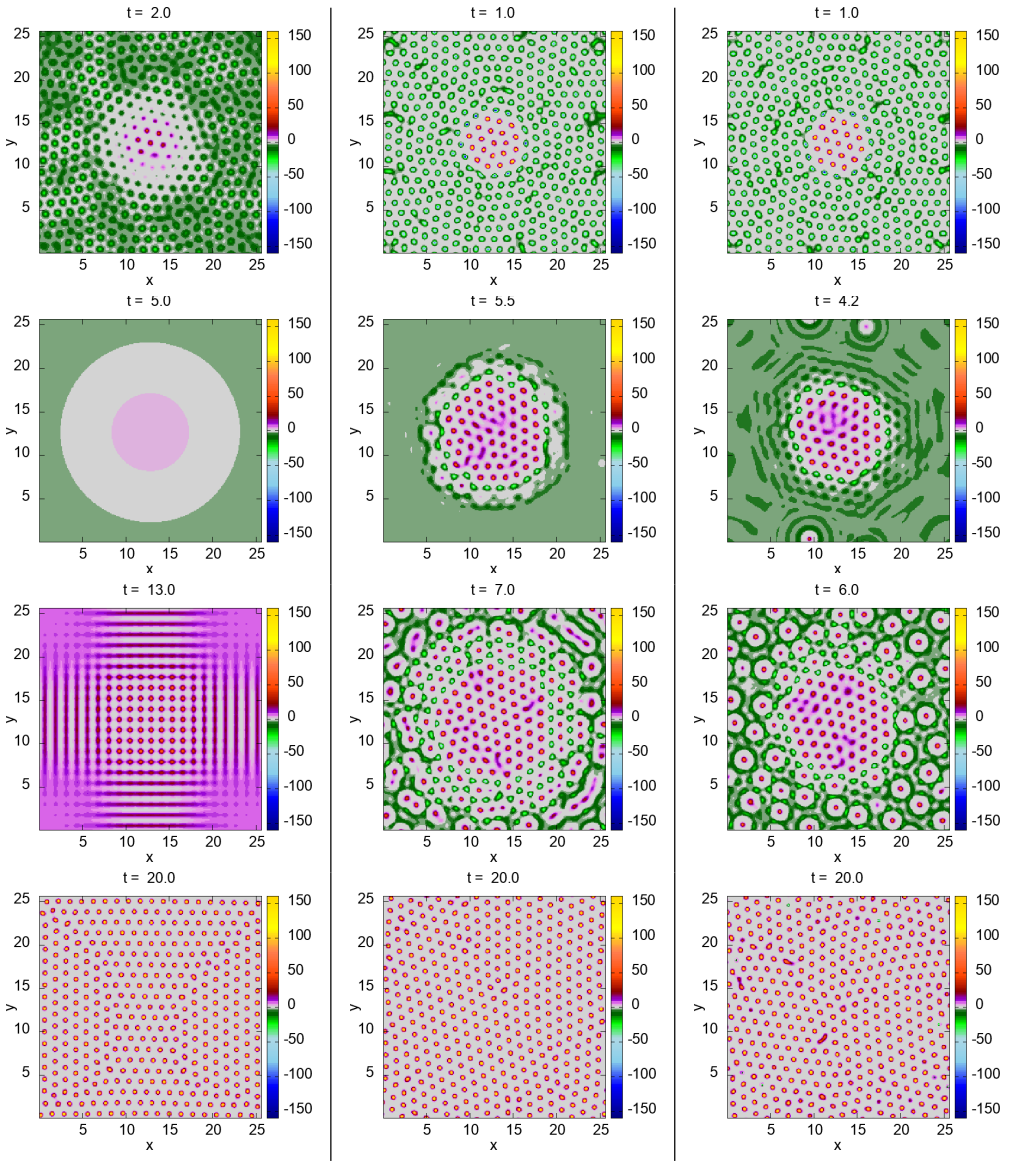

FIG. 11. Snapshots of $(\rho_1 - \rho_2)$, for various $\beta\varepsilon_{12} = 1$ (left), $\beta\varepsilon_{12} = 1.75$ (middle), and $\beta\varepsilon_{12} = 2$ (right) and various different times, with time increasing from top to bottom, as indicated above. The other pair potential parameters are $\beta\varepsilon_{11} = \beta\varepsilon_{22} = 1$, $R_{11} = R_{22} = 1$, and $R_{12} = 0.9$. The other model parameters are $\tilde{\lambda}_{n1} = \tilde{\lambda}_{n2} = 1$, $c_1 = c_2 = 0.5$, $\alpha = 2$, and $\tilde{S}_n = 9$ with $f(\mathbf{r}) = 1$. The area of the domain is 25.6×25.6 and $\Delta x = \Delta y = 0.1$.

increase the value $\beta\varepsilon_{12}$. For the results in the left hand column, which are for $\beta\varepsilon_{12} = 1$, there is no penetration of cancer cells into the healthy tissue. For $\beta\varepsilon_{12} = 1.75$ (middle column) the penetration starts at $t \approx 5.5$ whereas it begins at $t \approx 4.5$ for $\beta\varepsilon_{12} = 2$ (right hand column).

In Fig. 12 we plot the average densities of the cells and the nutrient as a function of time and also the trajectory of the system in the (ρ, ϕ) plane, corresponding to the results displayed in Fig. 11. This allows to see that the increased degree of "melting" at times $t \sim O(1)$ for smaller $\beta\varepsilon_{12}$ (particularly in the case with $\beta\varepsilon_{12} = 1$), is due to the fact that the linear stability threshold line is at higher total densities and is closer to the initial state. This means that the system spends a greater amount of time below the linear stability threshold line as it evolves along its trajectory in the (ρ, ϕ) plane. We also see from the plots of the average cell densities over time that the fluctuations over time in the density of the healthy cells increases with increasing $\beta\varepsilon_{12}$. In the (ρ, ϕ) plane, these fluctuations manifest as a meandering trajectory with zigzaglike portions.

Repeating the simulations corresponding to the results in Figs. 11 and 12, but using $R_{12} = 1.1$, such that $R_{12} > \frac{1}{2}(R_{11} + R_{22})$, and also $R_{12} = 1$, such that $R_{12} = \frac{1}{2}(R_{11} + R_{22})$, (results not displayed), we find that the results are qualitatively similar, but the melting phenomenon for $\beta\varepsilon_{12} = 1$ is prolonged for the smaller value of R_{12} and shortened for the larger value of R_{12}. Also, the time at which the cancer cells penetrating into the healthy tissue first appear is earlier for larger R_{12}.

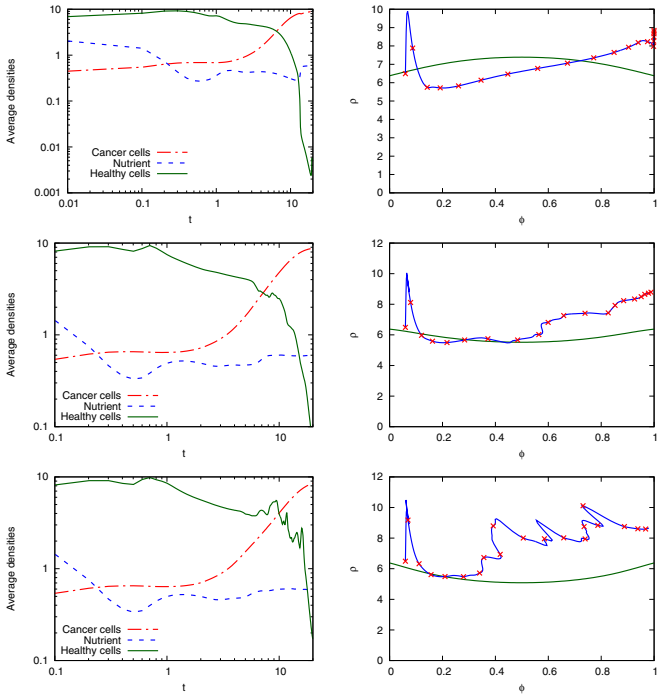

FIG. 12. On the left are plots of the average cell densities [see Eq. (10)] and the average nutrient density [see Eq. (11)] and on the right plots of the trajectory in the (ρ, ϕ) plane with the corresponding linear stability threshold line, corresponding to the results in Fig. 11. These are for varying $\beta\varepsilon_{12} = 1$ (top), $\beta\varepsilon_{12} = 1.75$ (middle), and $\beta\varepsilon_{12} = 2$ (bottom).

IV. CONCLUSIONS

In this paper we have incorporated DDFT to describe microscopic cell-cell interactions within a simple model of nutrient driven tissue growth. The theory was applied for a single cells type (Sec. II) and for two cell types (Sec. III), the latter representing, for example, the interaction between healthy and tumor cells; this approach can easily be generalised to describe more cell types. The resulting models consist of coupled integro-partial differential equations with nonlinear source terms describing nutrient driven growth. This level of description is common in discrete models, but their analysis is limited mainly to numerical simulation; one of the main advantages of the DDFT approach is that the model is amenable to mathematical analysis, providing greater insights into the nature of the numerical results. For instance, the linear stability analysis of Secs. II D and III C identify parameter regimes for which stable peaks arise, representing the locations of cell centres, as demonstrated in the simulations in Secs. II E and III D. While some parameters can be estimated readily from the experimental literature, this analysis also goes some way to estimate the DDFT associated parameters that are difficult to determine from direct measurements (e.g., the effective cell-cell cross interaction radius R_{12}). A further outcome of our linear stability analysis in the competition case, is the observation that as the cell radii ratio R_{22}/R_{11} is increased, the two wave numbers at which the system can become linearly unstable move apart leading to the linear stability threshold to develop a cusp. If the radii ratio is sufficiently large (a regime not explored in detail here) then the system can be linearly unstable at two quite different wave numbers and the interaction between these can produce a wide range of different structures [59,60,67], which are interesting from the pattern-formation perspective, and may also have some biological relevance.

There is still much required in the development of the basic theory before it can be applied directly to experimental results. However, the numerical results reflect qualitatively the expected results based on observation, despite the use of simple growth kinetics and interaction potentials. For example, the mean densities (a proxy for total number of cells) in Figs. 2 and 4 qualitatively resemble Gompertzian or logistic type growth curves often reported in tumor growth models [68]. A further noteworthy aspect of the model is the splitting events shown in Fig. 5, reflecting mitosis. We note also that for a uniform nutrient distribution, such events are not observed at very large times as the arrangement of the cells settles to a fixed configuration; such results are reflective of the cellular rest states observed in mature liver and muscle tissues.

In the simulations of Sec. III, the parameter values for the kinetics guarantee that the tumor cells will overrun the healthy cells. However, it is interesting that the manner by which this is done depends on the value of the interaction parameters R_{ij} and ϵ_{ij} and in particular the cross-interaction radius R_{12} and energy ϵ_{12}. Although the critical values for R_{12} suggested here are not strictly defined, it was found that (i) if $R_{12} < \frac{1}{2}(R_{11} + R_{22})$, i.e., the cross-species interaction range is less than mean of the two same-species interaction ranges, then tumor cells tended to penetrate the healthy regions, while (ii) if $R_{12} > \frac{1}{2}(R_{11} + R_{22})$ the tumor cells tend to displace the the healthy cells at the tumor edge, in accordance with the insight gained from studies of mixtures of soft particles [52–54,69,70]. Situation (i) is reminiscent of metastasis, while (ii) reflects a benign tumor state. Of course, some caution should be applied to such interpretations on the basis of the current analysis, but it is noteworthy that the DDFT approach does identify a potential behavioral property of the cells that can govern benign and virulent tumors. The present work also shows that the overall collective behavior is sensitive to the details of the pair interactions between cells.

The complex dynamics that the system can exhibit is rather striking. For instance, the drop in the nutrient level observed, e.g., in Figs. 8–10 that then leads to a drop in the overall number of healthy cells, which results in the "crystal" melting temporarily, which corresponds to the cells being distributed in disordered liquidlike configurations. The nutrient level then recovers and the system "refreezes" and subsequently over time the cancer cells penetrate the healthy tissue and eventually the healthy cells all die out.

The current work is the first to analyze a model using DDFT to describe the growth of tissues and tumors. There is considerable scope to extend the model to create a more realistic description of tissue growth. For example, a simple model of extra-cellular matrix (ECM) was proposed in Ref. [36], whereby ECM gradients generates a haptotactic response of cells, providing a further mechanism for cell movement and arrangement. Another aspect where the present model could be extended relates to the description of the cell-cell interactions. In the models here, these are treated via soft purely repulsive potentials. It would be interesting to compare results with those from alternative soft potential models such as that proposed

in Ref. [71]. However, in reality there is also attractions (adhesion) between cells, which points to the possibility of the analog of the gas-liquid or gas-solid phase transitions in collections of cells. Incorporation of both attraction and repulsion between particles in a DFT is straightforward [40–42], but the theory becomes much more elaborate, which is why we avoided such theories for this initial study. Despite the current model being very simplistic in comparison to many models of tumor growth, these initial results demonstrate that DDFT has considerable potential as an effective modeling approach to describe microscale cell-cell interactions that can provide new insights into the dynamics of tissue and tumor growth.

ACKNOWLEDGMENTS

A.A. acknowledges stimulating conversations with John Lowengrub, which helped initiate this work. H.M.Al-S. acknowledges the Iraqi Ministry of Higher Education and Scientific Research for financial support.

APPENDIX: ESTIMATES FOR PARAMETERS VALUES

Here we discuss in further detail what are suitable values to use for the parameters in our model. For the homogeneous system with uniform density, from Eq. (9) we obtain

$$\rho(t) = \rho_0 e^{(\lambda_m n^* - \lambda_d)t}, \tag{A1}$$

where ρ_0 is the initial density. For a given nutrient concentration n^* and assuming a 12-h doubling time [72], then from this we can deduce

$$(\lambda_m n^* - \lambda_d) = \frac{\ln 2}{12}\ \mathrm{h}^{-1}. \tag{A2}$$

According to Ref. [73], a typical value for the concentration of oxygen in fresh water $[O_2] = n^* = 6.383$ mg/L, so we estimate that the critical level n_d for $[O_2]$ is approximately $\frac{n^*}{20} = \frac{6.383}{20} = 0.32$ mg/L (equivalent to about 1% of atmospheric levels). Hence, $\lambda_m n_d - \lambda_d = 0$ leads to

$$\lambda_m = \frac{\lambda_d}{0.32\ \mathrm{mg/L}}, \tag{A3}$$

and on substitution into Eq. (A2) gives

$$\lambda_d = 0.00005\ \mathrm{min}^{-1},$$

hence

$$\lambda_m = 0.00015\ \mathrm{L min}^{-1}\mathrm{mg}^{-1}. \tag{A4}$$

The length scale R is the mean radius of the cells, so from Table I we have $R \approx 10\ \mu\mathrm{m} = 0.001$ cm and in two dimensions the typical diffusion distance in time t, is estimated from the two-dimensional average distance diffused squared over time formulas, $\langle r^2 \rangle = 4D_c t$. Assuming the time taken to travel a distance of order the diameter of the cell R is about 12 h, then

$$(2R)^2 = 4D_c \times 12\ \mathrm{h} \Rightarrow R^2 = 12D_c,$$

hence,

$$D_c = \frac{R^2}{12\,\mathrm{h}} = \frac{0.001^2}{12\times 60\,\mathrm{min}} = 1.3\times 10^{-9}\,\mathrm{cm}^2/\mathrm{min}.$$

The dimensionless population growth constant is $c_1 = \frac{R^2\lambda_d}{D_c}$, so we get $c_1 = 0.038$. From the definition of $\tilde{D}_c = \frac{D_n}{D_c}$, and $D_n = 2\times 10^{-5}\,\mathrm{cm}^2/\mathrm{s}\,(D_n = 1.2\times 10^{-3}\,\mathrm{cm}^2/\mathrm{min})$ [74,75], this leads to

$$\tilde{D} = \frac{12\times 10^{-4}}{13\times 10^{-10}} \approx 1\times 10^6. \tag{A5}$$

The nutrient source term $\tilde{S}_n = \frac{R^2 S_n \lambda_m}{\lambda_d D_c}$ is estimated to be $\mathrm{O}(10^6)$ so that in Eq. (15) $\bar{n}$ is in balance with the diffusion term. Hence, $\frac{3}{13}\times 10^4 S_n \approx (10^6) \Rightarrow S_n = 433$. From Eq. (15) we also see that the term involving $\tilde{\lambda}_n$ also must balance with diffusion, hence from Eq. (13) we see λ_n must be $\mathrm{O}(10^{-4})$ to ensure that $\tilde{\lambda}_n$ is of $\mathrm{O}(10^6)$. Recall that the number density is the number of cells per unit area $\rho = \frac{N}{A}$. Since $R \approx 10\,\mu\mathrm{m} = 0.001$ cm, this implies that the area covered by one circular cell $= \pi R^2 \approx 3\times 10^{-6}\,\mathrm{cm}^2$. This then implies that a typical cell density is $\rho \approx \frac{1}{3}\times 10^6\,\mathrm{cm}^{-2}$, i.e., $3\times 10^5\,\mathrm{cm}^{-2}$.

We summarize the values of dimensional parameters in Table I and dimensionless parameter values in Table II.

[1] H. M. Byrne, in *Proceedings of the 9th General Meetings of European Women in Mathematics* (2000), pp. 81–107.
[2] R. Siegel, C. DeSantis, K. Virgo, K. Stein, A. Mariotto, T. Smith, D. Cooper, T. Gansler, C. Lerro, S. Fedewa *et al.*, CA: Cancer J. Clinic. **62**, 220 (2012).
[3] R. Weinberg, *The Biology of Cancer* (Garland Science, New York, 2013).
[4] A. C. Burton, Growth **30**, 157 (1966).
[5] H. Greenspan, Stud. Appl. Math. **51**, 317 (1972).
[6] R. M. Sutherland, J. A. McCredie, and W. R. Inch, J. Natl. Cancer Inst. **46**, 113 (1971).
[7] L. Glass, J. Dyn. Syst. Meas. Control **95**, 324 (1973).
[8] W. S. Bullough, Cancer Res. **25**, 1683 (1965).
[9] J. P. Ward and J. King, Math. Med. Biol. **14**, 39 (1997).
[10] J. S. Lowengrub, H. B. Frieboes, F. Jin, Y. Chuang, X. Li, P. Macklin, S. M. Wise, and V. Cristini, Nonlinearity **23**, R1 (2009).
[11] J. A. Adam, Math. Biosci. **81**, 229 (1986).
[12] D. L. S. McElwain, R. Callcott, and L. E. Morris, J. Theor. Biol. **78**, 405 (1979).
[13] C. J. Breward, H. M. Byrne, and C. E. Lewis, Bull. Math. Biol. **65**, 609 (2003).
[14] M. E. Orme and M. A. J. Chaplain, Math. Comput. Model. **23**, 43 (1996).
[15] H. M. Byrne and M. A. J. Chaplain, Math. Biosci. **130**, 151 (1995).
[16] R. S. Kerbel, Carcinogenesis **21**, 505 (2000).
[17] C. Viallard and B. Larrivée, Angiogenesis **20**, 409 (2017).

[18] P. S. Kim, P. P. Lee, and D. Levy, Bull. Math. Biol. **70**, 1994 (2008).

[19] K. D. Miller, R. L. Siegel, C. C. Lin, A. B. Mariotto, J. L. Kramer, J. H. Rowland, K. D. Stein, R. Alteri, and A. Jemal, CA: Cancer J. Clinic. **66**, 271 (2016).

[20] J. P. Ward and J. R. King, Math. Biosci. **181**, 177 (2003).

[21] E. Ruoslahti, Sci. Am. **275**, 72 (1996).

[22] L. A. Liotta, J. Kleinerman, and G. M. Saidel, Cancer Res. **34**, 997 (1974).

[23] L. A. Liotta, J. Kleinerman, and G. M. Saldel, Cancer Res. **36**, 889 (1976).

[24] J. A. Adam, Math. Biosci. **86**, 183 (1987).

[25] C.-Y. Chen and J. P. Ward, Bull. Math. Biol. **76**, 3088 (2014).

[26] A. Pierres, A. M. Benoliel, and P. Bongrand, in *Cell-Cell Interactions, in Physical Chemistry of Biological Interfaces* (Marcel Dekker, New York, 2000), pp. 459–522.

[27] M. J. Piotrowska and S. D. Angus, J. Theor. Biol. **258**, 165 (2009).

[28] A. R. A. Anderson, Math. Med. Biol.: J. IMA **22**, 163 (2005).

[29] J. A. Engelberg, G. E. P. Ropella, and C. A. Hunt, BMC Syst. Biol. **2**, 110 (2008).

[30] D. Drasdo and S. Höhme, Phys. Biol. **2**, 133 (2005).

[31] J. Galle, M. Hoffmann, and G. Aust, J. Math. Biol. **58**, 261 (2009).

[32] J. Jeon, V. Quaranta, and P. T. Cummings, Biophys. J. **98**, 37 (2010).

[33] S. Turner, J. A. Sherratt, and D. Cameron, J. Theor. Biol. **229**, 101 (2004).

[34] A. F. M. Marée, V. A. Grieneisen, and P. Hogeweg, in *Single-cell-based Models in Biology and Medicine* (Springer, Berlin, 2007), pp. 107–136.

[35] A. Shirinifard, J. S. Gens, B. L. Zaitlen, N. J. Popławski, M. Swat, and J. A. Glazier, PLoS ONE **4**, e7190 (2009).

[36] A. Chauviere, H. Hatzikirou, I. G. Kevrekidis, J. S. Lowengrub, and V. Cristini, AIP Adv. **2**, 011210 (2012).

[37] U. M. B. Marconi and P. Tarazona, J. Chem. Phys. **110**, 8032 (1999).

[38] A. J. Archer and R. Evans, J. Chem. Phys. **121**, 4246 (2004).

[39] A. J. Archer and M. Rauscher, J. Phys. A: Math. Gen. **37**, 9325 (2004).

[40] R. Evans, Adv. Phys. **28**, 143 (1979).

[41] R. Evans, *Fundamentals of Inhomogeneous Fluids* (Dekker, New York, 1992), Chap. 3.

[42] J.-P. Hansen and I. R. McDonald, *Theory of Simple Liquids: With Applications to Soft Matter* (Academic Press, San Diego, 2013).

[43] C. N. Likos, Phys. Rep. **348**, 267 (2001).

[44] J. Dautenhahn and C. K. Hall, Macromolecules **27**, 5399 (1994).

[45] C. N. Likos, H. Löwen, M. Watzlawek, B. Abbas, O. Jucknischke, J. Allgaier, and D. Richter, Phys. Rev. Lett. **80**, 4450 (1998).

[46] A. A. Louis, P. G. Bolhuis, J.-P. Hansen, and E. J. Meijer, Phys. Rev. Lett. **85**, 2522 (2000).

[47] J. Dzubiella, A. Jusufi, C. N. Likos, C. von Ferber, H. Löwen, J. Stellbrink, J. Allgaier, D. Richter, A. B. Schofield, P. A. Smith, W. C. K. Poon, and P. N. Pusey, Phys. Rev. E **64**, 010401(R) (2001).

[48] I. O. Gotze, H. M. Harreis, and C. N. Likos, J. Chem. Phys. **120**, 7761 (2004).

[49] B. M. Mladek, M. J. Fernaud, G. Kahl, and M. Neumann, Condens. Matter Phys. **8**, 135 (2005).

[50] C. Likos, Soft Matter **2**, 478 (2006).

[51] D. A. Lenz, R. Blaak, C. N. Likos, and B. M. Mladek, Phys. Rev. Lett. **109**, 228301 (2012).

[52] A. J. Archer and R. Evans, Phys. Rev. E **64**, 041501 (2001).

[53] A. J. Archer, C. N. Likos, and R. Evans, J. Phys.: Condens. Matter **16**, L297 (2004).

[54] I. O. Gotze, A. J. Archer, and C. N. Likos, J. Chem. Phys. **124**, 084901 (2006).

[55] B. M. Mladek, D. Gottwald, G. Kahl, M. Neumann, and C. N. Likos, Phys. Rev. Lett. **96**, 045701 (2006).

[56] A. J. Moreno and C. N. Likos, Phys. Rev. Lett. **99**, 107801 (2007).

[57] S. D. Overduin and C. N. Likos, J. Chem. Phys. **131**, 034902 (2009).

[58] M. Carta, D. Pini, A. Parola, and L. Reatto, J. Phys.: Condens. Matter **24**, 284106 (2012).

[59] A. J. Archer, A. M. Rucklidge, and E. Knobloch, Phys. Rev. Lett. **111**, 165501 (2013).

[60] A. J. Archer, M. C. Walters, U. Thiele, and E. Knobloch, Phys. Rev. E **90**, 042404 (2014).

[61] C. M. O'Connor, J. U. Adams, and J. Fairman, *Essentials of Cell Biology* (NPG Education, Cambridge, MA, 2010).

[62] P. J. Mohr, B. N. Taylor, and D. B. Newell, J. Phys. Chem. Ref. Data **41**, 043109 (2012).

[63] A. C. Hindmarsh, *Scientific Computing* (North Holland, Amsterdam, 1983), Vol. 1, pp. 55–64.

[64] A. C. Hindmarsh, http://www.llnl.gov/CASC/odepack (2002).

[65] A. J. Archer, J. Phys.: Condens. Matter **17**, 1405 (2005).

[66] M. Derenzini, D. Trere, A. Pession, L. Montanaro, V. Sirri, and R. L. Ochs, Am. J. Pathol. **152**, 1291 (1998).

[67] A. J. Archer, M. C. Walters, U. Thiele, and E. Knobloch, in *Mathematical Challenges in a New Phase of Materials Science* (Springer, Berlin, 2016), pp. 1–26.

[68] M. Marušić, S. Vuk-Pavlovic, and J. P. Freyer, Bull. Math. Biol. **56**, 617 (1994).

[69] A. J. Archer, C. N. Likos, and R. Evans, J. Phys.: Condens. Matter **14**, 12031 (2002).

[70] S. D. Overduin and C. N. Likos, Europhys. Lett. **85**, 26003 (2009).

[71] D. Drasdo, S. Hoehme, and M. Block, J. Stat. Phys. **128**, 287 (2007).

[72] P. N. Werahera, L. M. Glode, F. G. La Rosa, M. S. Lucia, E. D. Crawford, K. Easterday, H. T. Sullivan, R. S. Sidhu, E. Genova, and T. Hedlund, Prostate Cancer **2011**, 301850 (2011).

[73] J. E. Sherwood, F. Stagnitti, M. J. Kokkinn, and W. D. Williams, Int. J. Salt Lake Res. **1**, 1 (1992).

[74] J. P. Ward and J. R. King, Math. Med. Biol. **16**, 171 (1999).

[75] J. P. Ward and J. R. King, J. Theor. Med. **1**, 287 (1999).